CARDIAC REGENERATION AND DISEASE MODELING USING BIOMATERIAL-FREE THREE-DIMENSIONAL (3D) BIOPRINTED CARDIAC TISSUE

by

Chin Siang Ong

A dissertation submitted to Johns Hopkins University in conformity with the
requirements for the degree of Doctor of Philosophy.

Baltimore, Maryland

March 2019

Abstract

Biomaterial-free 3D bioprinting is a relatively new field within 3D bioprinting. In this implementation, 3D tissues are created from the fusion of 3D multicellular spheroids, without requiring biomaterials. This is in contrast to traditional 3D bioprinting, which requires biomaterials to carry the cells to be bioprinted, such as a hydrogel or decellularized extracellular matrix. In this dissertation, we discuss the generation of biomaterial-free 3D cardiac spheroids and 3D bioprinted cardiac patches, their mechanical, electrical and biological functional characterization *in vitro* and *in vivo* for cardiac regeneration. Additionally, we investigated their potential use as a disease model using congenital long QT syndrome due to an inherited calmodulinopathy as an example, utilizing CRISPR interference to shorten abnormally prolonged cardiac action potentials. At the same time, we demonstrate the use of virtual reality for the interactive visualization of cardiovascular structures and its potential use in pre-surgical planning and patient-specific precision medicine.

Primary Reader: Andreas Barth, MD PhD

Secondary Reader: Daniel H. Reich, PhD

PhD Thesis Advisors: Gordon Tomaselli, MD, Narutoshi Hibino MD PhD

Acknowledgements

I would like to thank my PhD thesis advisors, Gordon F. Tomaselli and Narutoshi Hibino for their invaluable mentorship and support. I would like to thank my nuclear family (Sheryl Ang, Nathan Ong, Nicholas Ong), as well as my extended family (parents Hua Hui Ong, Sok Kheng Er and parents-in-law Steven Ang, Susan Soh) for their constant support, patience and understanding. I would like to thank my colleagues (Tomaselli lab: Deborah DiSilvestre, Chen Yu Huang, Jingnan Han, Roald Teuben, Ijala Wilson, Fede Farinelli; Hibino lab: Takuma Fukunishi, Tom Zhang, Andrew Nashed, Isaree Pitaktong, Yang Bai, Joseph Boktor, Enoch Yeung) and collaborators (Tung lab: Adriana Blazeski, Renjun Zhu). I would like to thank the Division of Cardiac Surgery and the Division of Cardiology at the Johns Hopkins Hospital, my PhD program (Cellular and Molecular Medicine: Rajini Rao, Robert Casero, Leslie Lichter, Colleen Graham) and mentors I have been fortunate to meet and work with, during my PhD (Duke Cameron, Glenn Whitman, Jennifer Lawton, Stefano Schena). Finally, I would like to thank the American Heart Association (AHA) for awarding me the AHA Predoctoral Fellowship (2017-2019) and the Tan Kah Kee (TKK) Foundation for awarding me the TKK Postgraduate Scholarship (2017).

Publications and Coauthors

Chapters 1-3:

Ong CS, Pitaktong I, Hibino N. Principles of spheroid preparation for creation of 3D cardiac tissue using biomaterial-free bioprinting. Book: 3-D Bioprinting: Principles & Protocols (Springer Nature) (2018). (1)

Ong CS, Fukunishi T, Nashed A, Blazeski A, Zhang H, Hardy S, DiSilvestre D, Vricella L, Conte J, Tung L, Tomaselli G, Hibino N. Creation of Cardiac Tissue Exhibiting Mechanical Integration of Spheroids Using 3D Bioprinting. J Vis Exp. 2017 Jul 2;(125). doi: 10.3791/55438. PubMed PMID: 28715377. (2)

Ong CS, Fukunishi T, Zhang H, Huang CY, Nashed A, Blazeski A, DiSilvestre D, Vricella L, Conte J, Tung L, Tomaselli GF, Hibino N. Biomaterial-Free Three-Dimensional Bioprinting of Cardiac Tissue using Human Induced Pluripotent Stem Cell Derived Cardiomyocytes. Sci Rep. 2017 Jul 4;7(1):4566. doi: 10.1038/s41598-017-05018-4. PubMed PMID: 28676704; PubMed Central PMCID: PMC5496874. (3)

Chapter 4:

Yeung E, Fukunishi T, Bai Y, Bedja D, Pitaktong I, Mattson G, Lui C, **Ong CS**, Matsushita H, Inoue T, Hibino N. 3D Printed Cardiac Patch Augments Angiogenesis and Reduces Scar Tissue Formation in Vivo. Southern Thoracic Surgical Association 65th Annual Meeting, November 7-10 2018, Amelia Island, FL. (4)

This project was initiated by **Ong CS** and was subsequently completed by Yeung E.

Ong CS, Fukunishi T, Pitaktong I, Hardy S, Zhang H, Huang CY, Vricella L, Tomaselli GF, Hibino N. Cardiac remuscularization using 3D bioprinted cardiac patches. Circulation 2017;136(Suppl 1):A15589-A15589. (5)

Ong CS, Fukunishi T, Zhang H, Huang CY, Blazeski A, DiSilvestre D, Vricella L, Tung L, Tomaselli GF, Hibino N. Improvement of electrophysiological and morphological characteristics of 3D bioprinted human induced pluripotent stem cell-derived cardiac patches by defined factors. Congenital Heart Surgeons' Society Annual Meeting. Chicago, IL;2017. (6)

Chapter 5:

Ong CS, Huang CY, Han J, Wilson I, Boktor J, Hibino N, Tomaselli GF. CRISPR interference to correct diseased 2D and 3D hiPSC-CMs with calmodulinopathies. Circulation 2018;138(Suppl 1):A11569-A11569. (7)

Chapter 6:

Ong CS, Krishnan A, Huang CY, Spevak P, Vricella L, Hibino N, Garcia JR, Gaur L. Role of virtual reality in congenital heart disease. Congenit Heart Dis. 2018 May;13(3):357-361. doi: 10.1111/chd.12587. Epub 2018 Feb 5. PubMed PMID: 29399969. (8)

Ong CS, Deib G, Yesantharao P, Qiao Y, Pakpoor J, Hibino N, Hui F, Garcia JR. Virtual Reality in Neurointervention. J Vasc Interv Neurol. 2018 Jun;10(1):17-22. PubMed PMID: 29922399 PubMed Central PMCID: PMC5999295. (9)

Ong CS, Faden M, Baschat AA, Garcia J, Miller JL. Virtual reality projection of fetal cardiac anomalies from three-dimensional prenatal ultrasound data. 28th World Congress on Ultrasound in Obstetrics and Gynecology (20-24 October 2018, Singapore). (10)

This thesis is a derivative work / compilation of multiple publications and conference proceedings of collaborative research works the author of this thesis (Ong CS) has taken part in during his PhD, rather than based on a single publication. For research works where the author of this thesis (CS Ong) is the first author or co-first author, content from these publications / conference proceedings are used, at times verbatim, at times with edits. For the single research paper (4), where the author of this thesis (CS Ong) initiated the study but the study was completed by another author (Yeung E), content, especially figures, are clearly attributed to the first author of the final manuscript (Yeung E), and the data is included with his permission, for completeness of discussion, at the request of the PhD Dissertation Committee. The author of this thesis (Ong CS) is a co-author on the eventual manuscript of this particular research paper.

For specific acknowledgements of each published collaborative research work, please refer to the published papers. For Chapter 5, which is at this time of writing unpublished, I would like to specifically acknowledge the assistance of Worawan Limpitikul who provided us with the iPSCs and her CRISPR interference constructs (11). Worawan Limpitikul had in turn obtained the iPSCs from Michael J. Ackerman from the Windland Smith Rice Sudden Death Genomics Laboratory, Department of Molecular Pharmacology and Experimental Therapeutics, Mayo Clinic, Rochester, MN earlier. I acknowledge Wanjun Yang for her aid in cell

culture, Adriana Blazeski and Renjun Zhu for their technical assistance in electrophysiological optical mapping. For Section 6.4, which is also at this time unpublished, I acknowledge the additional input of Rachel Chang and Lucy Nam, who joined the project after the abstract had been accepted.

Contents

List of Figures

Chapter 1

Introduction

1.1. Thesis Statement

Biomaterial-free 3D bioprinted cardiac tissues show promise for cardiac regeneration and cardiac disease modelling.

1.2. Motivation

Current treatments for heart failure, short of a heart transplant, do not address the fundamental issue of the loss of viable contractile cardiac tissue. Thus, cardiac stem cell therapy and cardiac tissue engineering have been developed. The generation of cardiac tissues may be performed with non-cellular biomaterials and without non-cellular biomaterials. The first half of this thesis focuses on creating biomaterial-free 3D bioprinted cardiac tissues using patient-specific human induced pluripotent stem cell derived cardiomyocytes and utilize these for cardiac regeneration.

Another important use of engineered cardiac tissues is for disease modeling and testing of therapeutic approaches to heart and vascular disease. The use of genome editing for correction of heritable heart disease has been hampered by inadequate organ and tissue models to assay efficiency of delivery and efficacy of therapeutics.

Clustered regularly-interspaced short palindromic repeats (CRISPR)/Cas9-mediated genome engineering offers a highly promising and specific method of correcting inherited gene mutations. This thesis explores using biomaterial-free 3D cardiac tissues to model congenital long QT syndrome and the possibility of gene correction using CRISPR interference.

1.3. Key Problems

Three dimensional (3D) cell culture and the creation of 3D multicellular spheroids have been around for almost five decades, but it is only recently, that spheroids are being employed increasingly for the purpose of tissue engineering (12) and tissue regeneration (13). 3D multicellular spheroids offer the opportunity to create 3D tissue without the use of biomaterials. Advances in 3D bioprinting technology have led to the new field of biomaterial-free 3D bioprinting (3, 14-18).

Traditional biomaterial-dependent 3D bioprinting (19) has limitations, such as the intrinsic stress to live cells by heat exposure or shear stress during 3D bioprinting, isolation of 3D bioprinted cells from their neighbors, and the risk of foreign material in the biomaterials, which may be relatively contraindicated for eventual intended clinical use. In contrast, using spheroids as building blocks for 3D bioprinting is gentler (19) and may recapitulate the developmental biological environment encountered early on, in the developing embryo.

1.4. Contributions

This thesis makes the following contributions:

In Chapter 2, we present the principles of spheroid preparation for creation of 3D cardiac tissue using biomaterial-free 3D bioprinting,

In Chapter 3, we present the generation of biomaterial-free 3D cardiac tissue using 3D bioprinting and characterized them in isolation and investigated their potential use as a disease model.

In Chapter 4, we present the utilization of these 3D patches for cardiac repair in three rodent surgical models, as ways of delivering cardiac stem cells to the heart.

In Chapter 5, we explore the use of biomaterial-free 3D cardiac tissue to model congenital long QT syndrome.

In Chapter 6, we explore the use of 3D segmentation, 3D printing and 3D virtual reality in cardiovascular medicine and demonstrate how patient-specific customized cardiac tissue with complex shapes and geometries can be created using biomaterial-free 3D bioprinting.

We summarize our findings in Chapter 7.

Chapter 2

Principles of spheroid preparation for creation of 3D cardiac tissue using biomaterial-free 3D bioprinting

2.1 Introduction

In this chapter, we discuss the principles and important considerations for creation of 3D cardiac tissue from multicellular spheroids using biomaterial-free 3D bioprinting based on our experience with the Regenova 3D bioprinter (Cyfuse Inc, Tokyo, Japan). We divide the protocol and principles into 4 distinct steps: Spheroid optimization (Step 1), spheroid dislodgement (Step 2), spheroid transfer (Step 3) and spheroid fusion (Step 4). These are important considerations for biomedical engineers, who seek to use existing spheroid-based 3D bioprinters and also create the next generation of spheroid-based 3D bioprinters.

2.2 Spheroid optimization / creation

The principle behind spheroid optimization is to create a 3D multicellular spheroid (Figure 1) that is:

- Not too adherent to the bottom of the ultra-low attachment U-well, that will result in significant effort during spheroid dislodgement (Step 2).

- Compact and strong enough to prevent disintegration during spheroid transfer (Step 3)
- Appropriately sized to ensure adequate fusion between spheroids (Step 4, Figure 2)

For this, the following parameters (non-exhaustive list) may be adjusted to obtain the optimized spheroid. Our parameters (3) are stated in parentheses.

- Type of cells (hiPSC-CMs, FBs, HUVECs)
- Cell ratio (CM:FB:EC 70:15:15)
- Number of cells seeded into 96-well plate for one spheroid (33,000 cells)
- Duration of 3D culture (72 hours)

The threshold of what is considered an optimized spheroid varies widely. For us, these are the parameters of the spheroid that we consider acceptable for bioprinting.

- Resultant spheroid diameter (500-600 μm)
- Resultant cell viability within spheroid (93.3%)
- Spheroid circularity/roundness (70%)
- Spheroid smoothness (70%)

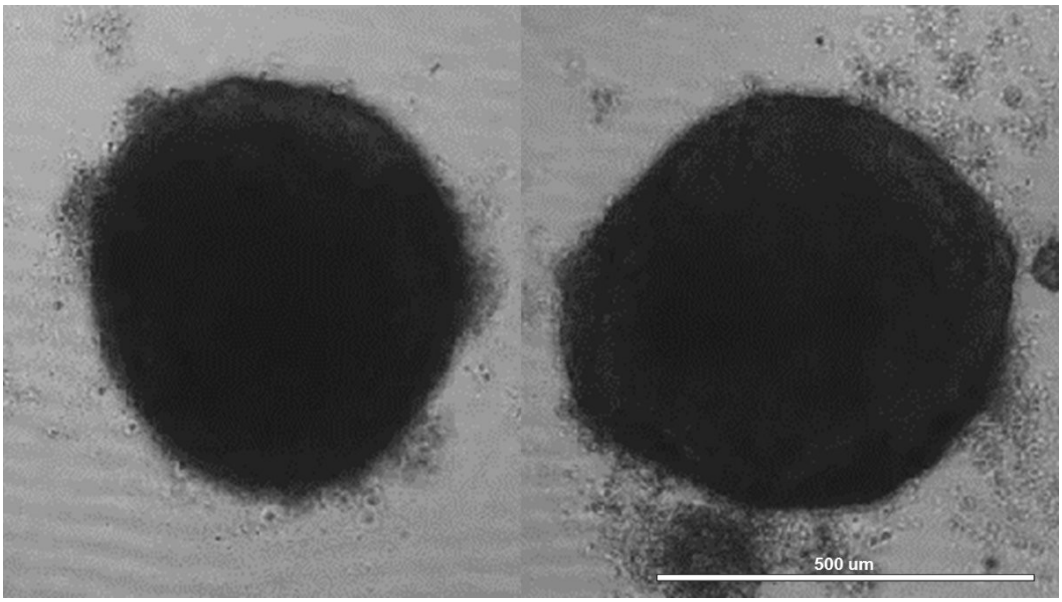

Figure 1: 3D cardiospheres. Cells in each well aggregate at the bottom of ultra-low attachment 96-well U-bottom plates to form spheroids by gravity. These spheroids can be visually inspected under light microscopy, where they should appear circular by two-dimensional projection (14).

2.3 Spheroid dislodgement

The principle behind spheroid dislodgement is that the spheroid created should be ideally as easy to pick up as possible, without the need for too much damage to the shape of spheroids in this process and troubleshooting. The following list includes what we usually consider when we seek to establish the optimal conditions for the dislodgement of spheroids.

- Spheroid culture conditions: We seek to optimize the spheroid culture conditions by modifying parameters as documented in the previous section. In addition, the type of cells (adult or neonatal), maturity/stemness (in the case of stem cells), passage number, timing of harvesting cells, culture duration, and culture medium (e.g. addition of growth factor) also affect the adhesion of spheroids to the bottom of the well. For example, from our experience, younger, immature hiPSC-CMs 3 weeks post-differentiation adhere better to each other and form spheroids faster, than older, more mature hiPSC-CMs 2-3 months post-differentiation. Spheroids made from younger, immature hiPSC-CMs also appear more compact. Spheroids that are cultured for a longer duration are more adherent to the bottom of the well.
- Cell types within the spheroids: Cell types are inherently different, and some cell types may secrete more extracellular matrix or be "stickier" or attaching to the bottom of the well, than others. For example, from our experience, reduction in the proportion of fibroblasts in the spheroid, in particular, can decrease the adhesion of spheroids to the bottom of the well. This parameter may be difficult to modify if a specific type of tissue with a specific cell type ratio is desired to answer a scientific question, and that resultant spheroid is inherently more adherent to the bottom of the well. Thus, other methods listed above and below have to be employed instead.

- Mechanical force (such as tapping, hitting) may be required to dislodge the spheroid from the bottom of the well.
- Addition of exogenous biomaterial: For situations where cells do not adhere well to each other despite supporting cells that secrete ECM such as fibroblasts, exogenous biomaterial may be needed for spheroid creation.

2.4 Spheroid transfer

There are several methods to transfer spheroids, such as by machine-generated mechanical suction or manual pipetting. The principle behind spheroid transfer is that the spheroids need to be sufficiently compact in order to be picked up and moved during bioprinting. The way to increase spheroid compaction is generally the opposite of what was discussed in previous section. For example, increasing culture duration and fibroblast cell ratio will lead to more compact spheroids, at the cost of the spheroids being more adherent to the bottom of the wells. This however, is not always the case, as how compact spheroids are really depends on the shape in which the spheroids form. While we hope that spheroids form as spheres and gradually compact, they may be more elliptical or "pancake"-like, especially if they were strongly adherent to the bottom of the well in the early stages of spheroid formation (first 24 hours), due to the cell types / viability of the cells that were used. Spheroid reoptimization may be needed, if this step fails on multiple occasions and there is an unacceptable proportion of spheroid losses.

2.5 Spheroid fusion

The spheroids must fuse in order to form an organized 3D tissue. Spheroid size may be one of the most important factors for the fusion of spheroids. The principles behind spheroid fusion are:

- There must be sufficient overlap of spheroids of at least 50 μm, if a hypothetical line is drawn connecting the centers of the two spheroids, when inspected from the top of the needle array (Figure 2), to begin the fusion process.
- If the spheroids are too large and there is too much overlap, adjacent spheroids may be pushed away from each other, resulting in the creation of disorganized and fragile tissue.
- There must be sufficient time for spheroids to fuse [we culture for 3 days].
- The fusion process can be impaired if there are misplaced or lost spheroids during 3D bioprinting.
- As the 3D bioprinting process is not completely sterile, we recommend the addition of antibiotics immediately after 3D bioprinting, such as Penicillin/Streptomycin or Normocin to reduce contamination during the fusion process. Antibiotics may be added during spheroid creation, if there are significant issues with contamination despite maximal precautions and the addition of antibiotics immediately after 3D bioprinting. We add Normocin at 1:500 to our cell media. However, the addition of antibiotics to cell culture media before 3D bioprinting and for long durations after the tissue has been

created and is stable (not disintegrating), is not recommended as this may lead to antibiotic resistant bacteria and long term Normocin exposure may harm the cells. The required accessories of the 3D bioprinter should be assembled before autoclaving to minimize handling after autoclaving for improved sterility.

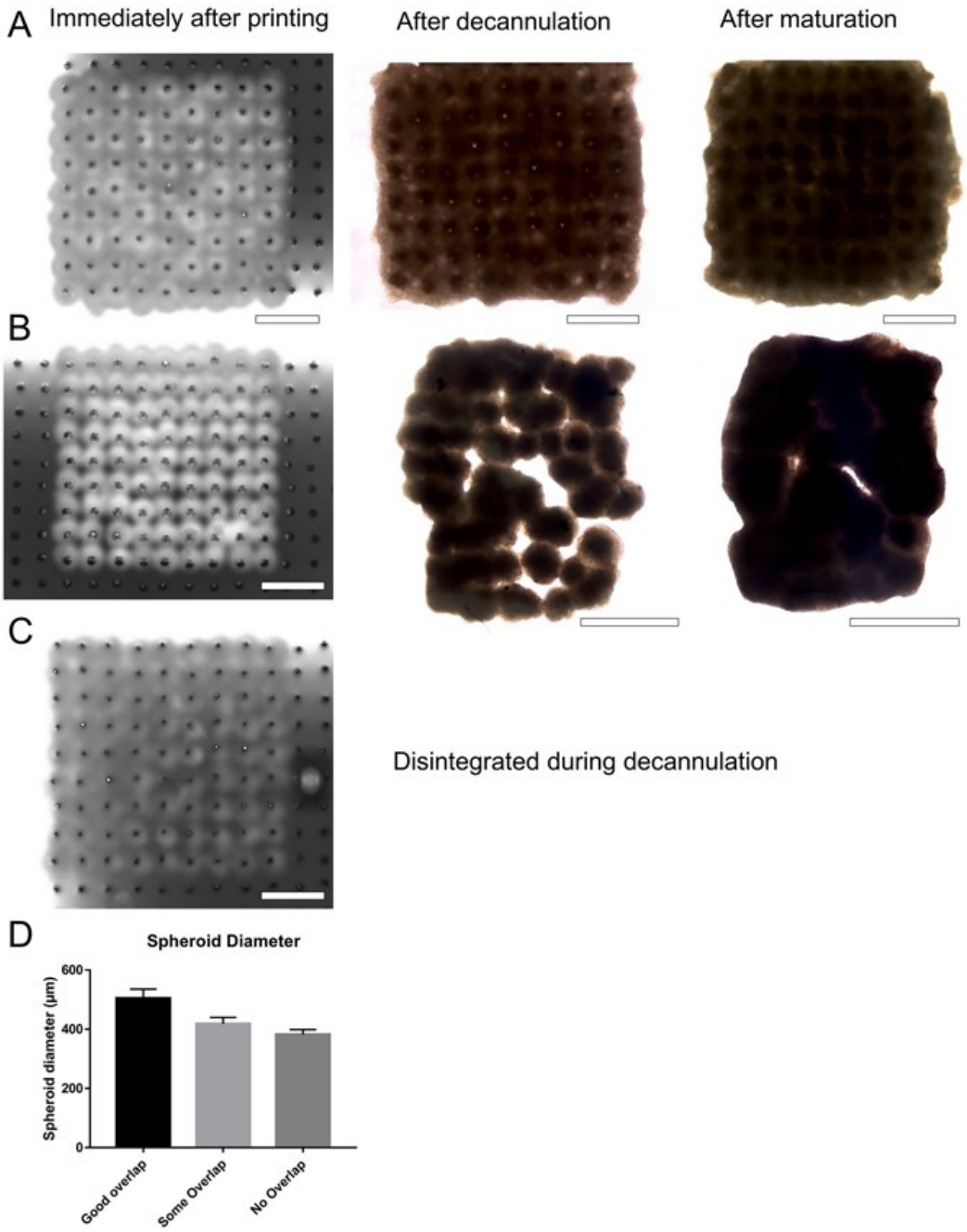

Figure 2: Cardiosphere dimensions and the degree of cardiosphere overlap determines the structural properties of 3D bioprinted cardiac patches. A-C:

Representative images of 3D bioprinted cardiac patches (CM:FB:EC 70:15:15) with overlap at least 50 μm (A), some overlap, 1 to 50 μm (B) and no overlap (C), immediately after printing, after decannulation and after maturation. Scale bar: 1000 μm. D: Cardiosphere diameters immediately before printing for 3D bioprinted cardiac patches in Panels A (504.6 ± 30.6 μm) (n = 81), B (413.1 ± 21.6 μm) (n=81), C (382.4 ± 16.1 μm) (n = 65) respectively (3).

2.6 Conclusion

A detailed laboratory protocol detailing every step with accompanying notes is available at the following reference (3), after more than 2 years of experience doing biomaterial-free spheroid-based 3D bioprinting. We have sought to document principles, tips and advice, discovered from repeated experimental trial and error, in detail. It is written in a spheroid-centric way, to emphasize the importance of the 3D cell spheroid as a transient building block, and the source of cells that comprise the final 3D bioprinted tissue construct, through the process of tissue engineering.

We suggest that the ideal process of tissue creation using biomaterial-free spheroid-based 3D bioprinting is based on the dynamic balance and flexible interactions of the four steps we have outlined. We use the Goldilocks principle in pursuit of the ideal spheroid for 3D bioprinting (not too small, not too large, not too compact, not too loose, etc.), while recognizing the inherent limitations of 3D culture, the 3D

bioprinter and the cell types to be bioprinted. This conceptual breakdown serves as a guide to understand the principles behind biomaterial-free spheroid-based 3D bioprinting and develop the next generation of 3D bioprinters.

There are also technical limitations in existing biomaterial-free 3D bioprinters that have not been covered in this chapter. For example, the fixed distance of 400 μm between adjacent needles inherently places the thickness of a 3D bioprinted single-layer patch to be around 500 μm, as that is the ideal spheroid diameter for 3D bioprinting (Figure 2). Improved temperature control, improved sterility within the 3D bioprinter, ability to self-sterilize, less reusable parts that require autoclaving, increased speed of the robotic moving equipment (Video B.1) and the ability to use culture media instead of PBS, are all factors that can improve 3D spheroid and 3D bioprinted patch viability, that might be helpful modifications for future generations of biomaterial-free 3D bioprinters.

Chapter 3

Generation of biomaterial-free 3D cardiac tissue and characterization in isolation and potential use as a disease model

3.1. Introduction

Heart failure is common, debilitating and ultimately lethal malady which consumes billions of dollars and thousands of lives each year (20). Current treatments for heart failure (21) alleviate symptoms and modestly prolong life but are palliative as they do not address the fundamental mechanism of the loss of functional cardiac tissue. Cellular therapy aimed at improving cardiac function and regenerating new myocardium, has been extensively investigated for cardiac repair (22). Despite numerous preclinical and clinical studies (23-28) performed to assess the ability of various stem cell populations to improve cardiac function and reduce infarct size, many important issues remain unresolved, and no cell therapy to date has been demonstrated conclusively to be effective. There are significant limitations to cell therapy in terms of cell retention, survival of the engrafted cells, cell differentiation, and integration of transplanted cells with host tissue (29).

In order to overcome the current issues in cell-based treatment of heart failure, the key challenges are: 1) Effective delivery of an abundant number of myocytes or

progenitor cells, 2) improvement of retention and engraftment of delivered cells with sufficient nutritional supply, 3) Development of biomaterial that can directly improve the contraction of cardiac tissue. Recent advances have applied 3D printing technologies to biocompatible materials, cells and supporting components with great promise for artificial organ printing and regenerative medicine applications (30). 3D bioprinting of myocardial tissue has utilized biomaterials (31, 32), such as polycaprolactone (PCL) (33), sodium alginate (34), 3D printed gelatin/methylbenzene sulfonate (MBS) extracellular matrix (ECM) scaffolds (35) or decellularized ECM to generate platforms for extrusion-based printing (36). The use of biomaterials faces challenges, such as immunogenicity, host inflammatory responses, fibrous tissue formation, biomaterial degradation and toxicity of degradation products, that affect the long term function of the engineered tissue construct (37).

We have developed a method to create 3D bioprinted cardiac tissue without the use of biomaterials (14) (Figure 3), by assembling multicellular cardiospheres consisting of human induced pluripotent stem cell derived cardiomyocytes (hiPSC-CMs), human adult ventricular cardiac fibroblasts (FBs) and human umbilical vein endothelial cells (ECs) using a 3D bioprinter. We hypothesize that novel biomaterial-free 3D printed cardiac patches will exhibit mechanical integrity with electrical integration of all the cell types of the cardiospheres.

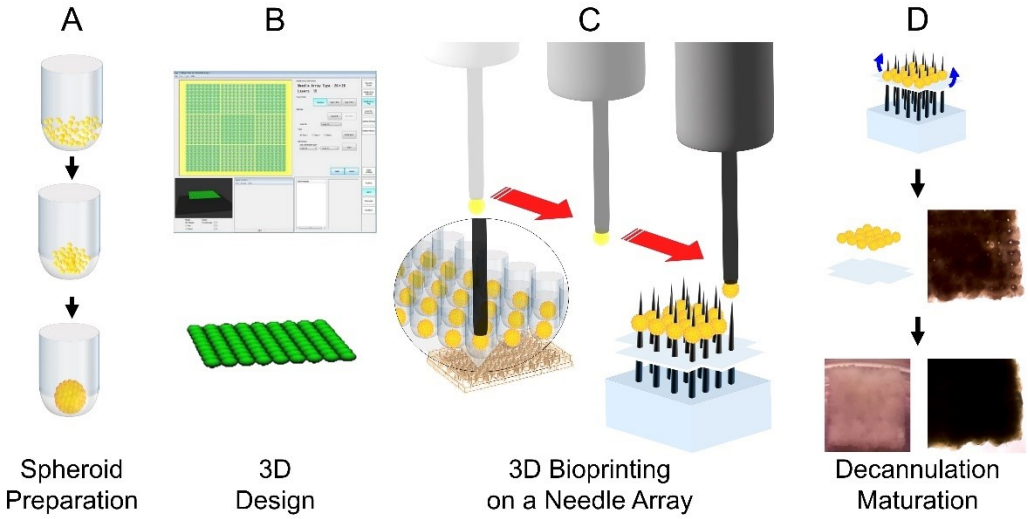

Figure 3: Schematic overview of biomaterial-free cardiac 3D bioprinting process. A. Cells (CMs, FBs, ECs) are aggregated in ultra-low attachment 96-well plates to form cardiospheres. B. The desired 3D structure to be bioprinted is designed using computer software. C. The 3D bioprinter picks up individual cardiospheres using vacuum suction and loads them onto a needle array. D. Cardiospheres are allowed to fuse. The 3D bioprinted cardiac tissue is then removed from the needle array and cultured further to allow the needle holes to be filled in by surrounding tissue.

3.2. Methods

3.2.1 Generation of hiPSC-CMs

Human IPSCs (reprogrammed from the peripheral blood mononuclear cells of a healthy donor) were differentiated into cardiomyocytes, by temporal modulation of Wnt signaling (38) using small molecules (CHIR99021, Tocris, R&D Systems, Cat.

No. 4423, and IWR-1, Sigma-Aldrich, Cat. No. I0161). We only used hiPSC-CMs from regions of 2D cultures that were beating to create cardiospheres. In addition, we also performed optical mapping on the hiPSC-CMs as 2D monolayers for quality control and to ensure that hiPSC-CMs were able to form electrical connections *in vitro* (see Supplementary Figure A.1, Video B.1).

3.2.2 3D bioprinting of cardiac patches

We have previously published our protocol for 3D bioprinting of cardiac patches using only cardiospheres, without the use of biomaterials (14) (Video B.2). In brief, hiPSC-CMs were co-cultured with human umbilical vein endothelial cells (Lonza, Cat. No. CC-2935) and human adult ventricular cardiac fibroblasts (FB) (Sciencell, Cat. No. 6310) for 72 hours to form mixed cell spheroids ("cardiospheres") (see Supplementary Figure A.2). A 3D bioprinter (Regenova, Cyfuse Biomedical K.K., Tokyo, Japan) was then used to construct biomaterial-free cardiac patches (Figure 3). The desired 3D geometry (one single layer of cardiospheres) was prepared using the 3D design software of the 3D bioprinter. The 3D bioprinter first identified the locations of the cardiospheres within U-wells of the ultra-low adhesion 96-well tissue culture plate by automated software detection. Then, a robotic arm used suction to pick up, transfer and load the cardiospheres individually onto a needle array in exact spatial coordinates, according to the pre-specified 3D design, in a sterile environment (see Supplementary Figure A.3). Each loading position was

calibrated by automated software-aided visual detection of the needle tips to ensure precision and accuracy. Once bioprinted, the cardiac patch was allowed to mature for 72 hours in culture with the needle array in place, while placed on a shaker (Compact Digital Microplate Shaker, Thermo Scientific, Waltham, MA) at 150 rounds per minute (rpm) in the incubator. During this time, the cardiospheres fuse. Then the needle array was removed (decannulation) and the cardiac patches were cultured for variable times before final evaluation and assessment.

3.2.3 Optical mapping

Cardiac patches were placed in a 35 mm dish and stained with 10 μM of the voltage-sensitive dye di-4-ANEPPS (Sigma-Aldrich Corp., St. Louis, MO) in Tyrode's solution (135 mM NaCl, 5.4 mM KCl, 1.8 mM $CaCl_2$, 1mM $MgCl_2$, 0.33 mM NaH_2PO_4, 5mM HEPES, and 5mM glucose (Sigma-Aldrich Corp., St. Louis, MO)), supplemented with 20 μM of the contraction inhibitor blebbistatin (Sigma-Aldrich Corp., St. Louis, MO) for 10 minutes at 37°C. Patches were rinsed twice with Tyrode's with blebbistatin before being transferred to a heated stage where they were allowed to equilibrate at 37°C for at least 5 minutes before the start of pacing. Samples were point paced with at least 30 stimulus pulses over a range of basic cycle lengths, starting from 2000 ms and decrementing until loss of capture. Optical recordings during pacing were obtained using a 100x100 pixel CMOS camera (MiCAM Ultima-L, SciMedia, Costa Mesa, CA).

Optical mapping data was analyzed using custom MATLAB scripts. Recordings at each pixel were de-noised using a previously described method (39) to regulate total signal variance and convolved with a 5x5 spatial Gaussian filter. Activation times, defined as the maximum of the derivative of membrane potential (dV/dt), were calculated as previously described (40). Histograms of local conduction velocities were generated for each patch and were fitted to a Gaussian curve. The mean of the Gaussian was defined as the average conduction velocity (CV). For each patch, action potential durations at 30 and 80 percent repolarization (APD_{30} and APD_{80}) were calculated for all local traces over the recording area and fit with Gaussian curves to determine the mean value for each sample, as described for CV measurements.

3.2.4 Flow Cytometry

Flow cytometry was performed on single cells dissociated from 2D hiPSC-CM monolayers using a flow cytometer (Accuri C6 Flow Cytometer, BD Biosciences, San Jose, CA) using the antibodies VCAM1, VEGFR2, PDGFRβ (BD Biosciences, San Jose, CA)

3.2.5 Immunofluorescence

Printed tissues were fixed in 4% paraformaldehyde, embedded in O.C.T. compound (Tissue-Plus™, Thermo Fisher, Waltham, MA), and cut into 8 μm sections. The

tissues were then washed in PBS, incubated in 0.5% Triton X for 5-10 minutes, washed in PBS again and blocked for one hour using 10% goat serum. Primary antibodies to the cell protein or biomarker of interest (Troponin, Alpha-Actinin, Connexin 43 (Cx43), Human Nucleic Acid (HNA), Wheat Germ Agglutinin (WGA)) were incubated with the sections overnight. Removal of unbound primary antibodies was accomplished by washing using PBS. Secondary antibodies were incubated with the sections for one hour before washing using PBS and mounting using Vectashield Antifade Mounting Medium with 4',6-diamidino-2-phenylindole (DAPI) (Vector Laboratories, Burlingame, CA).

3.2.6 Immunohistochemistry

High-temperature antigen retrieval and paraffin removal were performed by immersing slides in Trilogy (Cell Marque, Hot Springs, AR) in a pressure cooker until the chamber reached 126°C and 23 psi. A Dual Endogenous block (Dako, Carpinteria, CA) was applied for 5 minutes. Slides were incubated with antibodies to vimentin (Cell Signaling Technology, Danvers, MA), cardiac troponin T (Abcam, Cambridge, MA), or CD31 (Thermo Fisher, Waltham, MA), followed by addition of a mouse or rabbit HRP detection system (Leica Biosystems, Chicago, IL). Finally, slides were stained with a DAB substrate (Vector Lab, Burlingame, CA) and counterstained with hematoxylin (Richard-Allen Scientific, Kalamazoo, MI).

3.2.7 Cell Viability Assay

Cell viability of the 3D bioprinted cardiac tissue was determined using TUNEL assay (DeadEnd™ Fluorometric TUNEL System, Promega, Madison, WI) on 3D bioprinted cardiac tissue that was removed from cell culture media and immediately embedded in O.C.T. compound (Tissue-Plus™, Thermo Fisher, Waltham, MA), then cross-sectioned into 8 μm sections and stained. Live and dead cell counts were counted using ImageJ software on representative images in the periphery (n=4) and the center (n=4) of the 3D bioprinted cardiac tissue.

Cell viability of the cardiospheres was determined using a kit that marks live cells (the presence of ubiquitous intracellular esterase activity enzymatically converts nonfluorescent cell-permeant calcein AM to green fluorescent calcein) and dead cells with (ethidium homodimer enters dead cells with damaged membranes and binding to nucleic acids with red fluorescence) (LIVE/DEAD® Viability/Cytotoxicity Kit for mammalian cells #L3224, Thermo Fisher, Waltham, MA). Imaging of cardiospheres was then performed using a confocal laser scanning microscope (Zeiss LSM800 with upgraded GaAsP detectors).

Cell viability of the cardiospheres was also measured using a 3D cell viability assay (CellTiter-Glo #G9681, Promega, Madison, WI). Briefly, the spheroids/cells were mixed vigorously with the CellTiter-Glo 3D reagent for 5 minutes and incubated at

room temperature for 25 minutes to stabilize luminescence. It was then read by a plate reader (Molecular Devices Spectra MAX Gemini EM).

3.2.8 Imaging

Photographs of 3D bioprinted cardiac tissue and the 3D bioprinting process were acquired using an 8 MP digital camera. 3D bioprinted cardiac patches were imaged using inverted microscopes (EVOS XL, EVOS FL Cell Imaging System, Thermo Fisher, Waltham, MA). Confocal microscopy was performed using an upright Zeiss LSM 700 or LSM 510 Meta with oil-immersion objectives ranging from 40× to 63× using spectral lasers at 405-, 488- and 561-nm wavelengths. ImageJ software (NIH, Bethesda, MD) was used to generate composite microscopy images by combining fluorescent channels.

3.2.9 Statistics

For all experiments, data was represented graphically as bar or line charts with error bars, representing the mean with the standard error of the mean, using Prism 7 (GraphPad, La Jolla, CA). Statistical analysis of CV, APD, minimum pacing cycle length and cell viability was performed with unpaired 2-tailed t-tests. A p value less than 0.05 was considered statistically significant.

3.3.Results

3.3.1 hiPSC-CMs and cardiosphere formation

We generated hiPSC-CMs that were enriched for CM cell surface markers, as demonstrated by flow cytometry performed on hiPSC-CMs 14 days post differentiation (Figure 4). VCAM1, a cardiomyocyte marker (41), was predominantly expressed (93.2%). Of the 6.8% remaining cells, 1.8% and 1.4% were positive for the vascular and fibroblast markers VEGFR-2 and PDGFRβ. Further hiPSC-CM quality control measures (spontaneous beating phenotype, electrical connections by voltage optical mapping) are described in Methods.

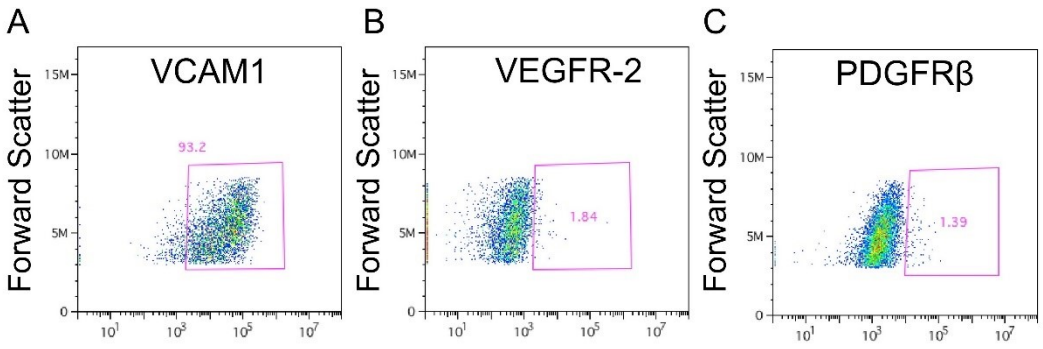

Figure 4: Cell surface markers expressed by hiPSC-CMs used to generate cardiospheres. A-C: Flow cytometry analysis using VCAM1 (A), VEGFR-2 (B), PDGFRβ (C) surface markers.

In order to create cardiospheres that were amenable to 3D bioprinting, we had to optimize the cell types, cell ratios and total cell numbers required for aggregation in each well. A fixed endothelial cell component of 15% was chosen based on a

previous report demonstrating prevascularization of cardiac patches using endothelial cells (42). Cardiospheres did not form when only hiPSCs or hiPSC-CMs were used; (Supplementary Figure A.2, Figure 5A-B). In the case of hiPSCs (Figure 5A), a loose, soft, gel-like cell aggregate, that is easily disrupted, formed within 48 hours. In the presence of FBs and ECs, hiPSC-CMs formed cardiospheres in 24 hours and these cardiospheres started beating spontaneously by 48 hours (Figure 5C-D). The spheroid beating rate was 28.7 ± 7.9 beats per minute (mean ± SD) (Figure 5E-G). We then created cardiospheres of different cell ratios (CM:FB:EC 85:0:15, 70:15:15, 45:40:15) and various cell densities (5, 10, 20, 30, 40, 60 thousand cells/cardiosphere), and measured their diameters after 3 days of culture (Figure 5H) and 5 days of culture (Figure 5I), to determine the mean cardiosphere diameters respectively.

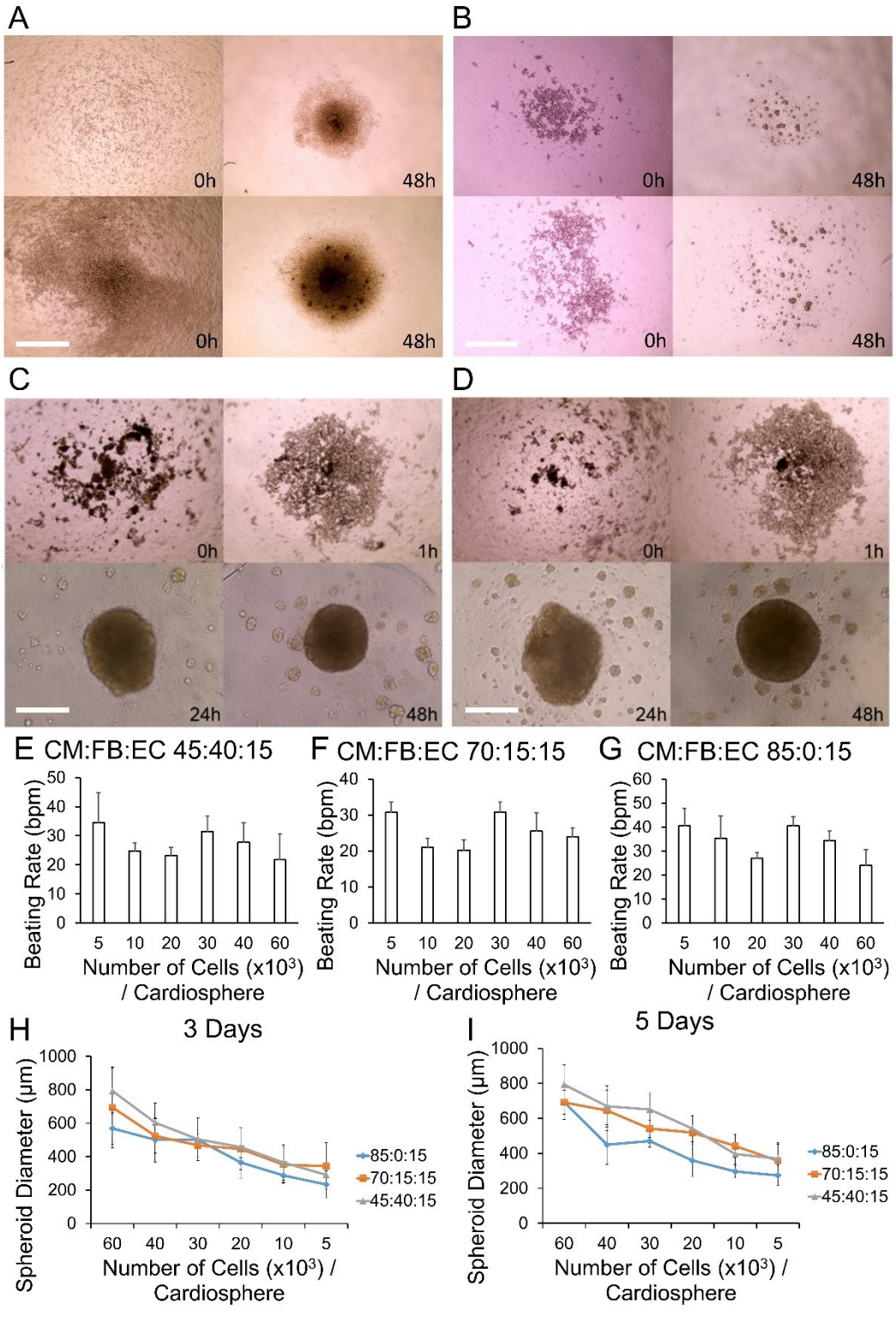
A
0h
48h
0h
48h
B
0h
48h
0h
48h
C
0h
1h
24h
48h
D
0h
1h
24h
48h
E CM:FB:EC 45:40:15
F CM:FB:EC 70:15:15
G CM:FB:EC 85:0:15
Beating Rate (bpm)
Number of Cells (x10³) / Cardiosphere
5 10 20 30 40 60
H 3 Days
I 5 Days
Spheroid Diameter (µm)
Number of Cells (x10³) / Cardiosphere
60 40 30 20 10 5
85:0:15
70:15:15
45:40:15

Figure 5: Cell type, number and ratio determine cardiosphere integrity. A-B: hiPSCs (100%) (A) and hiPSC-CMs (100%) (B) do not form spheroids after 48 hours in ultra-low attachment 96-well plates (Top 10,000 cells/well. Bottom 40,000 cells/well). C-D: hiPSC-CM:FB:EC ratio 70:15:15 (C) and 45:45:10 (D): Cardiospheres form in 24 hours and start beating in 48 hours. Scale bar panels A-D: 400 μm. E-G: Beating rate of cardiospheres composed of hiPSC-CM:FB:EC ratio of 45:40:15 (E), 70:15:15 (F) and 85:0:15 (G) at various cell numbers per cardiosphere, in beats per minute (bpm). H-I: Mean diameter (μm) of cardiospheres of various cell ratios (hiPSC-CM:FB:EC) and various cell numbers, after 3 days (H) and 5 days (I) of culture.

Sufficient overlap of cardiospheres was needed to form mechanically stable 3D bioprinted cardiac patches (Figure 2A-B, Figure 6). When the borders of the cardiospheres did not overlap sufficiently, the subsequent fusion of cardiospheres was poor and, upon decannulation from the needle array, the patches tended to disintegrate (Figure 2C). Interestingly, even though there were holes and partial disintegration of the patches, the unfused areas of the patches filled in and fused subsequently in culture after decannulation to form an intact patch, though the final patch size was smaller with an altered shape. Combining information about the amount of cardiosphere overlap needed (Figure 2D) with data about cardiosphere dimensions (Figure 5H-I), we chose to use 33,000 cells per cardiosphere for all

subsequent 3D bioprinting experiments, to create cardiospheres between 500 to 550 μm in diameter, that had sufficient overlap for mechanical integrity of the 3D bioprinted cardiac patches. Further assessment of cell viability of the cardiospheres (33,000 cells per cardiosphere, CM:FB:EC ratio 70:15:15) can be found as Supplementary Figure A.4.

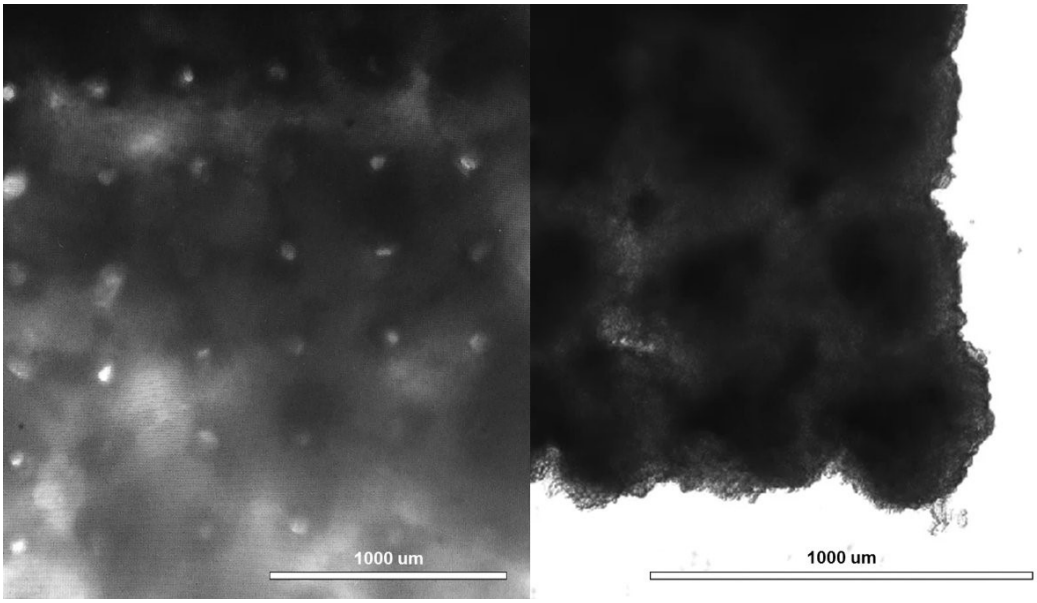

Figure 6: Creation of 3D cardiac patches exhibiting mechanical integration of spheroids. A 3D bioprinted cardiac patch immediately after removal from the needle array with visible needle holes (left). At this time, the boundaries between the spheroids had already become indistinct and the patch had already begun beating spontaneously, thus the spheroids had become mechanically integrated. Three days after removal from the needle array, the tissue voids caused by the

needle array were filled in by surrounding tissue (right), and the patch continued beating spontaneously. Scale bar: 1 mm.

3.3.2 Electrophysiological studies of 3D bioprinted cardiac patches.

It has previously been shown that the proportion of cardiomyocytes within a cardiosphere is directly proportional to the dimensional change of the cardiosphere during contraction and the addition of fibroblasts to the cardiospheres improves printed patch integrity (42). We were interested in the effect of fibroblasts on electrophysiological properties of 3D bioprinted patches, thus we chose three groups of cell ratios to study (CM:FB:EC ratio of 70:0:30, 70:15:15 and 45:40:15).

3D bioprinted cardiac patches of CM:FB:EC cell ratios 70:15:15 and 70:0:30 could be paced from a point source with electrical capture and propagation across the entire patch, as indicated by isochronal activation maps obtained by voltage optical mapping one week after bioprinting (43) (Figure 7A-B) (n=10). When a CM:FB:EC cell ratio of 45:40:15 was used, functional block in the middle of the patch, with slower conduction was occasionally observed (Figure 7C) (n=3). Conduction velocity (CV), APD_{30} and APD_{80} (44) were calculated for patches (CM:FB:EC 70:0:30 and 70:15:15) at pacing cycle lengths ranging from 2000 to 600 ms (Figure 7D-G). Patches with CM:FB:EC ratio of 45:40:15 were excluded due to the presence of occasional functional block (Figure 7C). CV tended to be slower in the

70:15:15 group (n=6), compared to the 70:0:30 group (n=4) but this did not reach statistical significance (Figure 7E). APD_{30} were significantly longer in the 70:15:15 group (n=6), compared to the 70:0:30 group at the longer pacing cycle lengths (n=4) (Figure 7F). APD_{80} was significantly longer in the 70:15:15 group (n=6), compared to the 70:0:30 group at all pacing rates (n=4) (Figure 7G). The minimum pacing cycle length producing capture was not statistically different between the 70:15:15 group and the 70:0:30 group (Figure 7H). The data are consistent with differing degrees of electrical integration in patches of different cellular composition.

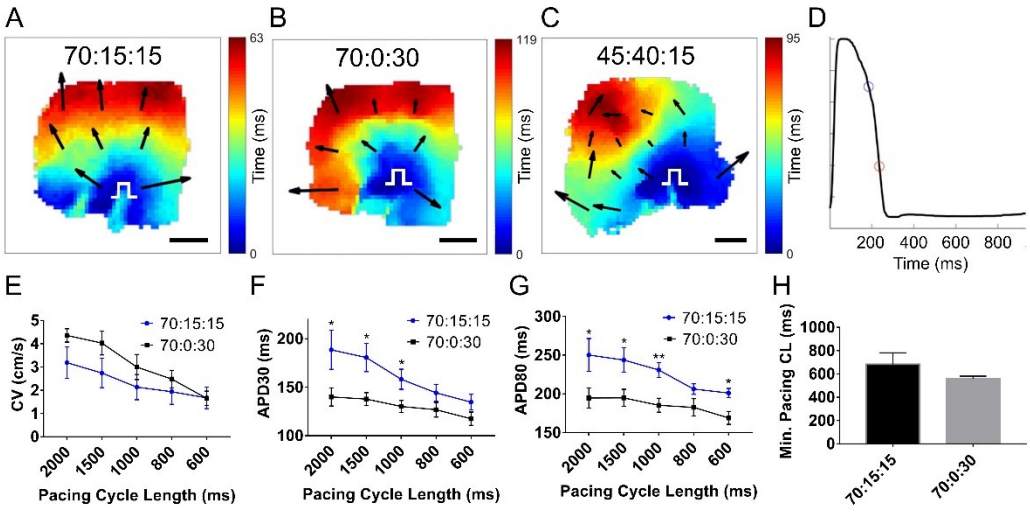

Figure 7: Optical mapping of 3D bioprinted cardiac patches demonstrates electrical integration of component cardiospheres. A-C: Representative isochronal activation maps of 3D bioprinted cardiac patches with CM:FB:EC ratios of 70:15:15, 70:0:30 and 45:40:15, respectively. White pulse symbol indicates site of the stimulus electrode. Arrows indicate vector magnitude and direction of activation. Scale bar:

1 mm. D: Representative action potential recording of a 3D bioprinted cardiac patch, with the circles indicating APD_{30} (blue circle) and APD_{80} (red circle). E-H: Mean conduction velocity (E), APD_{30} (F), APD_{80} (G) and minimum pacing cycle length (CL) with 1:1 capture (H) of 3D bioprinted cardiac patches (n=10).

3.3.3 Imaging of 3D bioprinted cardiac patches.

The electrophysiological data suggest high cell viability and TUNEL staining demonstrates a mean cell viability of 93.3 ± 5.4% one week after bioprinting (Figure 8A). At this time, the 3D cardiac patches stain positively for markers of each cell type that was incorporated into the cardiospheres: troponin T for CMs, vimentin for FBs and CD31 for ECs (Figure 9A-C). Interestingly, the pattern of CD31 staining suggests the formation of rudimentary blood vessels (Figure 9C). Histological stains (H&E and Masson Trichrome) of 3D bioprinted cardiac patches illustrate the presence of collagen indicating the deposition of extracellular matrix after printing of the patch (Figure 9D-E). Confocal microscopy revealed the presence of connexin 43 (Cx43), a gap junction protein that allows for electrical coupling between cardiomyocytes, localized to cell-cell borders between troponin T (Figure 8B) and alpha-actinin (Figure 8C) positive hiPSC-CMs. The distribution of the total number of cells is also comparable between the periphery and the center of the 3D bioprinted cardiac tissue (p=0.16) (see Supplementary Figure A.5).

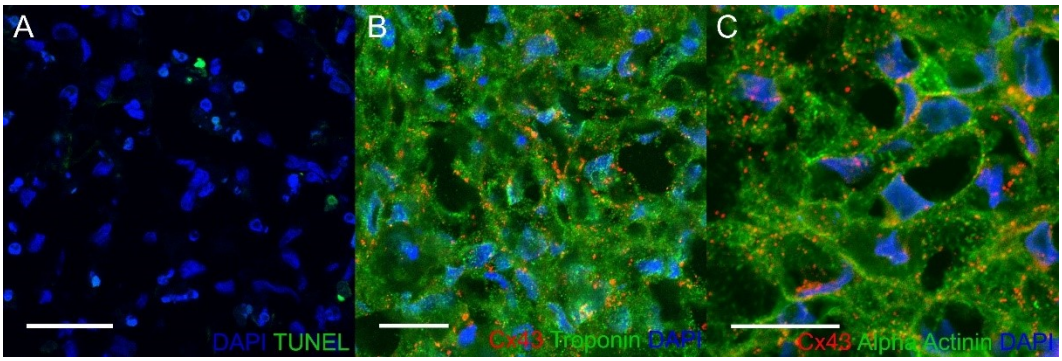

Figure 8: Confocal microscopy of 3D bioprinted cardiac patches. Immunofluorescence of 3D bioprinted cardiac patches (CM:FB:EC 70:15:15) using confocal microscopy. A: TUNEL (Green) DAPI (Blue), Scale bar: 40 µm. Mean patch viability (Live cells/Total cells) = 93.26 ± 5.42% (Mean ± SD). B: Cx43 (Red), troponin T (Green), DAPI (Blue). Scale bar: 20 µm. C: Cx43 (Red) Alpha-actinin (Green) DAPI (Blue), Scale bar: 20 µm. Troponin and α-actinin staining demonstrate the development of sarcomeres. Cx43 exhibit punctate staining and clusters of protein at cell contacts.

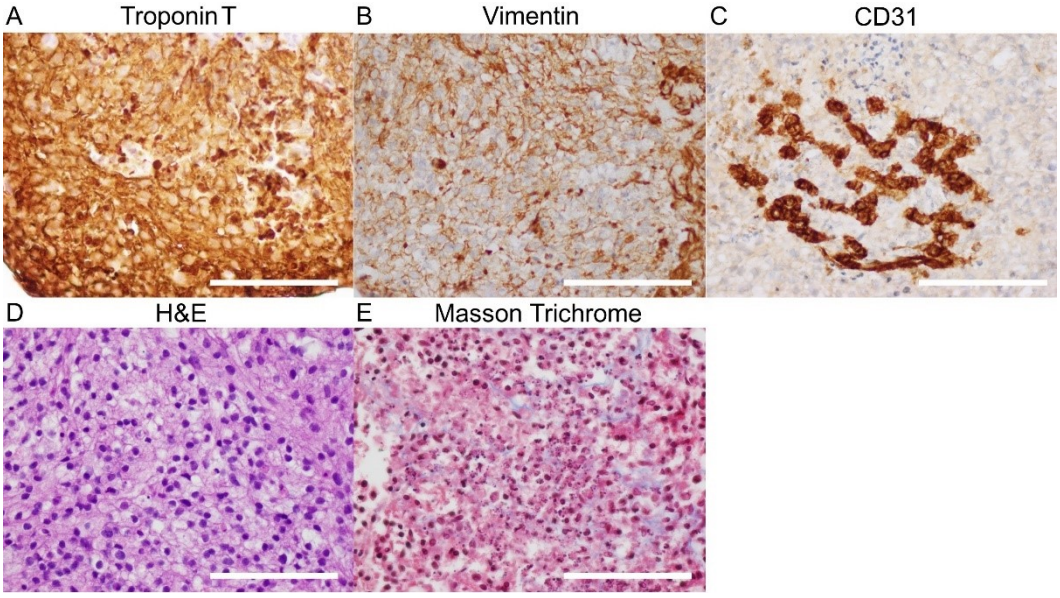

Figure 9: Immunohistochemistry and histology of 3D bioprinted cardiac patches. Tissue staining of 3D bioprinted cardiac patches (CM:FB:EC 70:15:15) with antibodies to troponin T (A), vimentin (B) and CD31 (C). D: H&E and E: Masson Trichrome stain. CD31 staining suggests the formation of rudimentary blood vessels. The tissues are highly cellular and Masson stain reveals the presence of fibrous tissue in the matrix. Scale bar: 100 µm.

3.4. Discussion

Biomaterial-free 3D printing of cardiac tissue avoids the problems associated with using biomaterials (37) (immunogenicity, fibrous tissue formation, biomaterial degradation, toxicity of degradation products), and also overcomes the difficulties of using cardiosphere self-assembly (42). It may be difficult to individually place

cardiospheres, as well as control the distance between cardiospheres by previously described methods. If cardiospheres are too far apart, tissue voids will be created in the final construct. On the other hand, if cardiospheres are too close together, they may stack and create areas in the patch with increased thickness.

Using our method, we were able to position cardiospheres in precise coordinates, in a flexible grid configuration (Figure 2), bioprinting patches of uniform shape and thickness (Figure 2A-B, Supplementary Figure A.3). This results in a more uniform tissue at the macroscopic and microscopic level, compared to previous reported random self-assembly of cardiospheres (42). Continuous electrical conduction (Figure 7A, B) also suggests uniform cardiosphere integration.

In the case of cardiosphere self-assembly (42), it may also be difficult to select individual cardiospheres. Our method allows for the selection of individual cardiospheres, for example, we can instruct the bioprinter to only use cardiospheres between 450 μm to 550 μm in diameter for bioprinting and reject the use of all others that do not fit this criterion. In addition, 3D bioprinting allows for complex 3D constructs of various geometries (e.g. tubes, rings, etc.) and thicknesses (number of layers) to be created, as well as 3D constructs made of cardiospheres of different cell types, cell ratios and total cell numbers. These complex shapes and structures may be difficult to create using other forms of biomaterial-free cardiac

tissue engineering, such as cell sheet technology (45-48), bioreactor culture systems (49, 50), including rotating orbital shakers (51, 52), rapid inter-cell click ligation process (53) and cardiosphere self-assembly (42).

In spite of the absence of biomaterials, we were able to achieve high cell density and functional cell contacts, creating a spontaneously beating cardiac tissue. Within 3 days of printing, our 3D bioprinted cardiac patches were spontaneously beating (while on the needle array), and after removal from the array, within another 2 days, the voids in the patch fused and the cardiospheres were electrically integrated (Figure 7). Due to the absence of exogenous biomaterials in our 3D bioprinted cardiac patches, the local 3D microenvironment may be more physiological (54, 55), and allow for more cell-cell coupling and communication.

The printed patches reveal high cell density; however, a potential drawback is low viability of cells in the bioprinted tissue due to lack of vascularization. Importantly, we have demonstrated the presence rudimentary blood vessel formed by ECs in the 3D bioprinted cardiac patches (Figure 9C) with a cell viability in the patch exceeding 90% (Figure 8A).

We recognize concerns regarding diffusion limitation. While the 3D bioprinted cardiac patches are histologically and electrically viable, and cell viability

measured at a single point in time is high, this does not imply that there is no cell death and cell turnover. It is possible that several tissue related factors improve oxygen and nutrient diffusion including spontaneous contraction of the patches, the presence of primordial vasculature (formation of primitive blood vessel-like structures), less compaction (especially immediately after printing) and prevascularization of the cardiospheres (inclusion of ECs in spheroids) (42). The cells in the cardiospheres may also exhibit greater tolerance to lower oxygen tension and hypoxic conditioning (56).

In forming cardiospheres (42, 57), two important factors must be considered: 1) the ratio of cell types, and 2) cell number. Cardiospheres were not formed when iPSCs or hiPSC-CMs alone were used (Figure 5A-B); in contrast, wells containing cardiomyocytes co-cultured with at least 15% ECs or FBs formed spheroids (Figure 5C-I). We kept the EC proportion constant at 15% on the basis of previous reports of successful prevascularization of cardiac patches using ECs as a component (42). Cardiosphere dimensions depended on cell number and varied slightly with cell composition (Figure 5). After optimization, we chose to use 33,000 cells per cardiosphere, to produce cardiospheres that overlap and form patches consistently (Figure 2, Figure 5G, H). We found that an overlap of 50 μm, on each side of the cardiosphere, i.e. cardiosphere diameter of 500 μm, allows for sufficient contact

between cardiospheres and for an intact cardiac patch to form 3 days after printing (Figure 2A).

Fibroblasts may help to stabilize patch structure, but these cells are likely to impact myocyte contacts and slow CV. In 3D bioprinted cardiac patches with a higher fibroblast ratio, there is lower CV, and significantly longer APD_{30} and APD_{80} (Figure 7F-G), suggesting that fibroblasts inhibit electrical coupling of myocardial cells. We also noted the presence of functional block (see Video B.3) and arrhythmic activity in the middle of the patches with higher fibroblast numbers. A recent study reported similar findings of prolonged APD and increased arrhythmogenicity in *in vitro* cultures of embryonic stem cell-derived cardiomyocytes co-cultured with adult cardiac fibroblasts, compared with co-culture with mesenchymal stem cells (58). Nonetheless, a non-myocyte cell source, such as fibroblasts, is needed to produce ECM. hiPSC-CMs and ECs will suffice in creating 3D bioprinted cardiac patches, but the slow elaboration of matrix by ECs results in friable patches that cannot be implanted. From a regenerative and biomimicry point of view (59, 60), the presence of both fibroblasts and endothelial cells is needed, and these cell types have been traditionally used by cardiac tissue engineers (61), attempting myocardial regeneration.

The optical mapping results corroborate the confocal imaging finding, which shows the presence of connexin 43 (Cx43), the main connexin in ventricular myocardium allowing for electrical coupling, expressed between troponin T and alpha-actinin positive hiPSC-CMs (Figure 8B-C). The absence of other biomaterial in biomaterial-free 3D printing of cardiac patches, may have facilitated the more rapid development of cell-cell contacts containing Cx43 and support more rapid propagation of activation through the patches.

The limitations of our study include the short-term culture of our 3D bioprinted cardiac patches, the relatively slow conduction velocity of the patches due to immaturity of hiPSC-CMs, and the weak mechanical properties of the 3D bioprinted patches. The 3D bioprinted patches consisted of a single layer of spheroid and the properties of a multi-layer thick patch could be different.

In conclusion, the generation of 3D bioprinted patches created with hiPSC-CMs derived from healthy control subjects is promising as a platform for cardiac tissue repair. The potential to take a patient's own cells (skin or peripheral blood), reprogram them to hiPSCs then differentiate the hiPSCs to cardiomyocytes is fundamental to the field of regenerative medicine. We have demonstrated it is feasible to 3D print biomaterial-free cardiac tissue patches using hiPSC-CMs. Biomaterial-free 3D printed cardiac tissue created from hiPSCs exhibited

spontaneous beating, electrical integration of component cardiospheres, and ventricular myocyte-like cellular electrophysiological properties. This constitutes a significant step towards a new generation of stem cell treatment for heart failure for tissue regeneration.

Chapter 4

Utilization of 3D cardiac patches to deliver cardiac stem cells to the intact heart for cardiac repair

4.1. Introduction

There are several methods to deliver cardiac stem cells to the heart, for cardiac regeneration after myocardial infarction (62). Before the advent of tissue engineering, the most common method was cell injection, but this was hampered by significant cell loss due to poor cell retention (63). Tissue-engineered cardiomyoplasty has been proposed as one of the methods to overcome the significant limitation of cardiac stem cell injection (64), as a next-generation therapy for cardiac repair (63).

Relevant to the field of tissue engineering in general, significant factors to consider in the intelligent design of any tissue, including cardiac tissue, blood vessels (65), etc., include cell source (stem cells (66), mature cells, none), the scaffold (natural, synthetic, none), and fabrication method, as these will affect the tissue viability, paracrine secretion, mechanical integrity and electrical conductivity of the final tissue construct. Particularly relevant to cardiac tissue, is electrophysiological function. A transplanted 3D cardiac patch that is not well connected can be a

substrate for arrhythmia development due to conduction delay and block. Scarring secondary to low tissue viability of any transplanted 3D cardiac patch can also lead to arrhythmia development and sudden cardiac death. Whilst there are already a number of studies looking at *in vivo* implantation of cell spheroids (13), there are far more limited studies examining *in vivo* implantation of 3D cardiac patches.

In this chapter, we look at the clinical translational value of biomaterial-free 3D cardiac patches, using 3 different rodent surgical models.

4.2. In vivo implantation of 3D cardiac patches on intact hearts

Animal procedures were reviewed and approved by the Johns Hopkins University Institutional Animal Care and Use Committee and performed in accordance with relevant institutional and federal guidelines and regulations for the care and use of laboratory animals. Nude rats (NIH RNU sp/sp rats, NTac:NIH-*Foxn1*^{rnu}, 12 weeks, female, 165-195 g, Taconic) were anesthetized using isoflurane, intubated and mechanically ventilated. A median sternotomy was performed and hemostasis was secured. A single cardiac patch was implanted directly onto the heart and secured with tissue glue and sutures. The chest was closed under aseptic technique and the animals were monitored for recovery from surgery. Animals were sacrificed 1 week after patch implantation and their hearts were explanted. Hearts were

sectioned along the short axis and embedded in O.C.T. compound or paraffin, for further histology and immunostaining.

3D bioprinted cardiac patches were implanted onto nude rat hearts (n=4) (Figure 10A-C) and remain engrafted on rat hearts 1 week after implantation (Figure 10D-F). Imaging of sections through the patch and native heart tissue reveals viable cells in the patch along with erythrocytes (Figure 10D, left, 3 white arrows), suggesting vascularization. Collagen staining is also present in the patch (Figure 10E, left). Confocal microscopy reveals presence of human nucleic acid (HNA)-positive cells in native rat myocardium, suggesting engraftment (Figure 10F, right, white arrow).

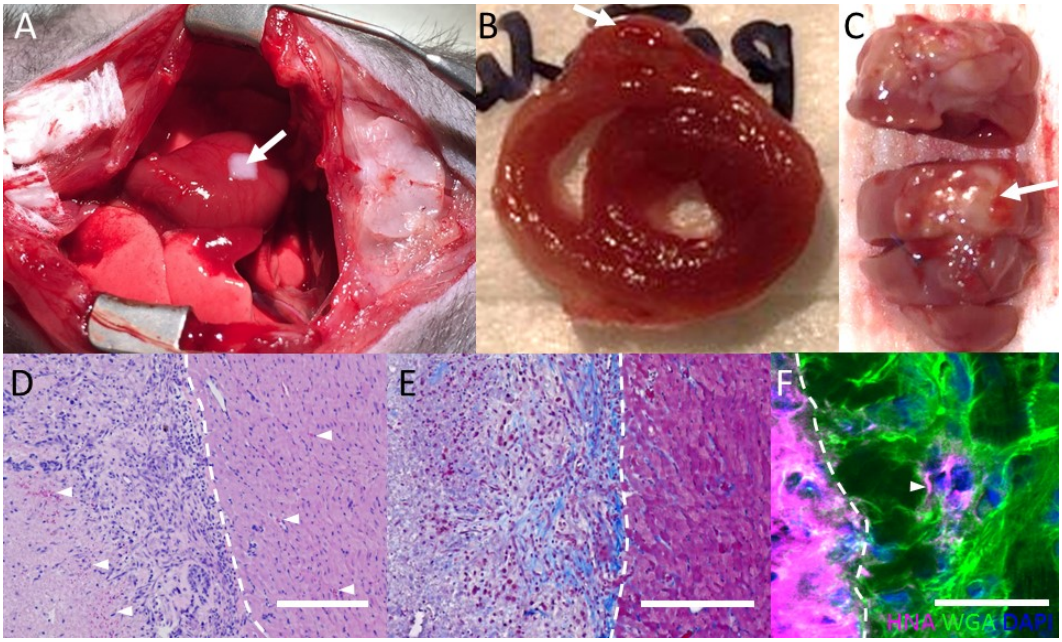

Figure 10: *In vivo* implantation of 3D bioprinted cardiac patches. A: Transplantation of 3D bioprinted cardiac patches (CM:FB:EC 70:15:15) onto the

anterior surface of the rat heart. B: Explanted heart (cross-section) C: Explanted heart (anterior aspect). D: H&E, white arrows indicate presence of erythrocytes. Scale bar: 400 μm. E: Masson Trichrome. Scale bar: 400 μm. F: Human Nuclear Antigen (HNA) (Magenta), Wheat Germ Agglutinin (WGA) (Green), DAPI (Blue). Scale bar: 40 μm. White arrows indicate presence of human cells in native rat myocardium. D-F: White dotted line demarcates the cardiac patch (left) from native rat myocardium (right).

In vivo implantations of 3D bioprinted cardiac patches onto nude rat hearts

(Figure 10) suggested vascularization and engraftment of 3D bioprinted cardiac patches, highlighting the promise of biomaterial-free 3D printing of cardiac tissue in myocardial regeneration and repair. Long term follow-up and functional analysis of the heart will be needed to show the efficacy of these 3D bioprinted cardiac patches. Notably, the purpose of the *in vivo* experiments was to optimize the conditions for engraftment and vascularization *in vivo*, as a proof of principle. Future studies involving vascularization, different culture conditions and modulation of the tissue with mechanical or electrical stimulation, and implantation in a myocardial injury model, amenable to therapeutics, to assess improvement in function, will be required to more completely assess this technology.

4.3. *In vivo* implantation in setting of myocardial infarction

As an extension of the study in the previous section where 3D bioprinted cardiac patches are implanted on intact hearts, this section (Attribution: Yeung et al (4)) follows with a functional study in the setting of a surgically created myocardial infarction by ligation of the left anterior descending (LAD) coronary artery in the same nude rat species. It is noted that the cardiac patch is retained *in situ* 4 weeks after surgery with high viability (Figure 11), decreased scar area (Figure 12), and improved vascularization (Figure 13), though there is no significant change in cardiac function and left ventricular mass (Figure 14).

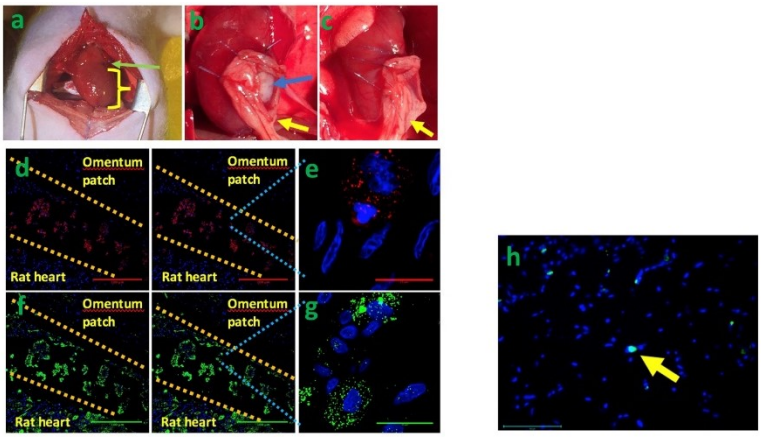

Figure 11: In vivo implantation of 3D cardiac patches in rodent LAD ligation model: Viability (A) Occlusion of the distal left anterior descending coronary artery, suture (green arrow), infarcted area (yellow) (B) Cardiac patch (Blue arrow) and omentum patch (yellow arrow) implantation in experiment group (n=6) (C) Omentum patch implantation only in sham group (n=6) (D-E) Evidence of retention

of the cells in rat 4 weeks after surgery, HNA (red), DAPI (blue), D: scale bar = 100 um, E: scale bar = 25um (F-G) Evidence of retention of the cells in rat 4 weeks after surgery, TropT (green), DAPI (blue), F: scale bar = 100um, G: scale bar = 25um (H) TUNEL staining of patch 4 weeks after surgery, dead cells are indicated by the yellow arrow), scale bar = 100um. (Figure attribution: Yeung et al (4))

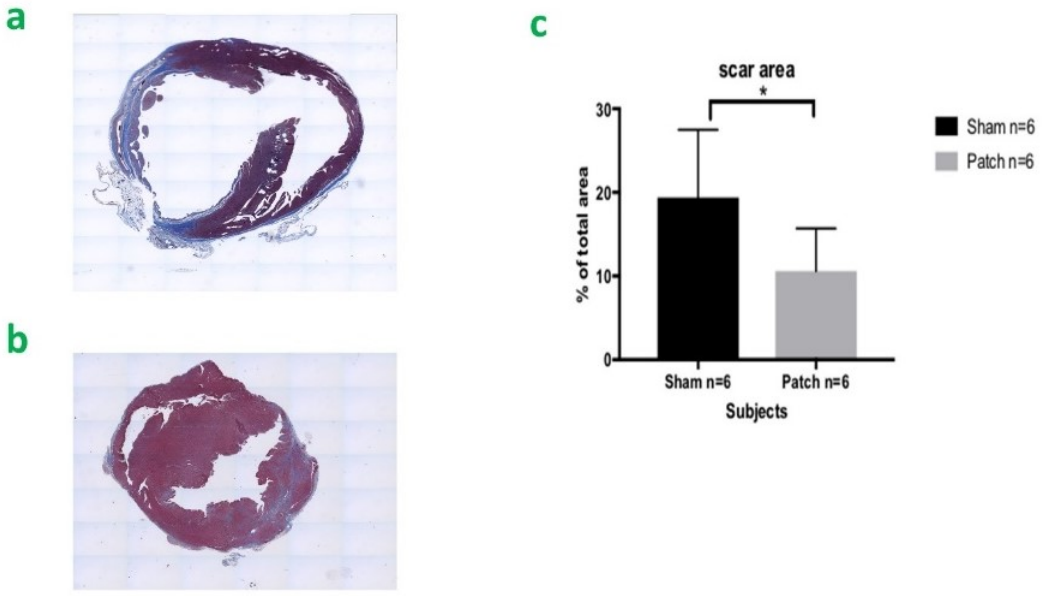

Figure 12: In vivo implantation of 3D cardiac patches in rodent LAD ligation model: Scar area A. Masson Trichrome staining of Sham group. B. Masson Trichrome staining of Patch group (Blue = infarcted area) C. Statistical analysis of scar area (percentage = blue / total area) ($p= 0.048$) (Figure attribution: Yeung et al (4))

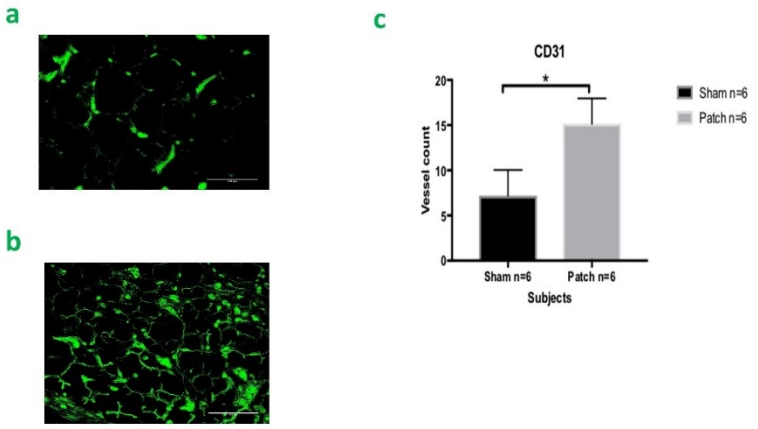

Figure 13: In vivo implantation of 3D cardiac patches in rodent LAD ligation model: Vascularization (A) CD 31 staining of Sham group, scale bar = 100um (B) CD31 staining of Patch group, scale bar = 100um (C) Statistical analysis of vessel counting (p = 0.001) (Figure attribution: Yeung et al (4))

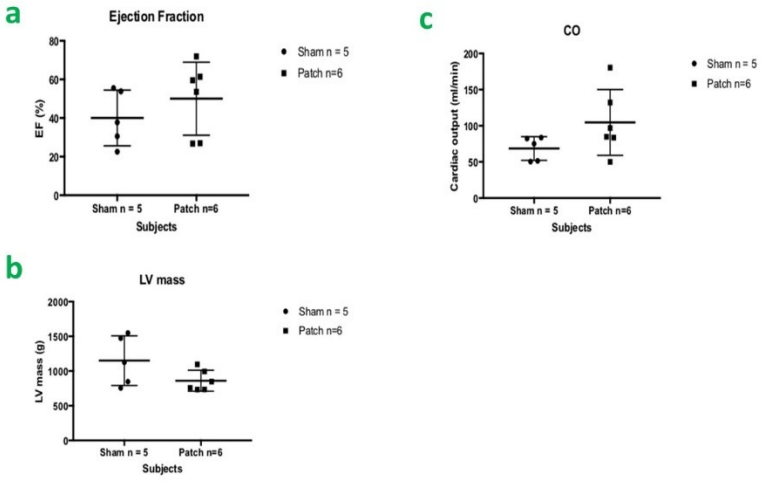

Figure 14: In vivo implantation of 3D cardiac patches in rodent LAD ligation model: Cardiac function (A) Left Ventricular Ejection Fraction, (B) Left Ventricular Mass, (C) Cardiac Output (Figure attribution: Yeung et al (4))

4.4. Transmural 3D cardiac patch implantation / "Dor" patch

Many studies examining cardiac regeneration using tissue engineered cardiac patches employ an epicardial approach in part to facilitate the assessment of vascularization and engraftment (3, 42, 52). In the previous chapters and sections, we have demonstrated the 3D bioprinting of biomaterial-free cardiac patches, made using human induced pluripotent stem cell-derived cardiomyocytes (hiPSC-CMs) (3, 14), which exhibit electrical and mechanical integration. These patches were subsequently implanted epicardially. The purpose of this study is to evaluate the feasibility of performing cardiac repair using reinforced, biomaterial-free 3D bioprinted full-thickness cardiac patches, akin to an endoventricular circular patch plasty or a Dor procedure (67), pioneered by French cardiac surgeon Vincent Dor in 1985, except that instead of a Dacron patch, a reinforced 3D bioprinted cardiac patch is used.

Biomaterial-free 3D bioprinted cardiac patches were engineered as previously described (3). To withstand ventricular pressures, the 3D bioprinted cardiac patches were first mechanically supported between 2 fibrin sheets (12-layers thick respectively) created using electrospinning (Figure 15A-B). Full-thickness defects were then surgically created in the right ventricles of nude rats (NIH RNU sp/sp rats, NTac:NIH-*Foxn1*^{rnu}, Taconic) (n = 5) (68) (Figure 15C-E). A pursestring suture is first made over the right ventricle (RV) and tightened to create an

outpouching of the RV. The RV is then incised. To ensure that a transmural defect is created, we made sure there was backflow of blood observed when we loosened the pursestring. The 3D bioprinted cardiac patch is then used to fill the defect and a PTFE patch is sutured on top of that, to further reinforce the tissue.

One month after implantation, we explanted and sectioned the heart to examine the implanted tissue, noting that grossly, the 3D bioprinted cardiac patch remained in situ (Figure 15F-H), with extracellular matrix present on Masson Trichrome staining (Figure 16A). In addition, there were red blood cells (Figure 16B, black arrows) in the 3D bioprinted cardiac patches on hematoxylin and eosin (H&E) staining, and CD31 positive blood vessels in the 3D bioprinted patches, consistent with vascularization of the graft (Figure 16C). The surgical RV defect made was filled with troponin-, alpha actinin- and human nuclear antigen- (HNA) positive cells, indicating the implanted 3D bioprinted patches remained viable (Figure 16D).

Interestingly, we note the presence of DAPI (4',6-diamidino-2-phenylindole) positive, HNA negative cells in the 3D bioprinted patches, suggesting the migration of rodent cells into the 3D bioprinted patches (Figure 16E, blue arrows). Also, we note the presence of HNA positive cells outside the 3D bioprinted patches (Figure 16E, yellow arrows), indicating the migration of human cells from the 3D bioprinted patches into the rodent myocardium. Echocardiography performed just

before explant indicated that the left ventricular ejection fraction was 73% and the right ventricular function was preserved.

These findings suggest that the 3D bioprinted patches we implanted contributed to tissue replacement of the heart. The surgical transmural defect allowed access to RV chamber blood supply to 3D cardiac patches, as compared to epicardial implantation, promoting the long-term survival of the patches.

In summary, we demonstrate the feasibility of full-thickness cardiac tissue replacement using 3D bioprinted cardiac patches in a novel rat model, with nascent vascularization and engraftment of the implanted tissue. The unique combination of hiPSC technology and 3D bioprinting technology allows for the possibility of patient-specific re-muscularization in patients with ischemic heart disease, using patient-specific hiPSC-CMs. The full thickness cardiac repair, in particular, may have implications for the treatment of transmural myocardial infarction in the future. Further studies evaluating the electrophysiological and mechanical integration of the 3D bioprinted patches *in vivo*, as well as the contractile function of these 3D bioprinted patches and scaling up to large animal models, are needed.

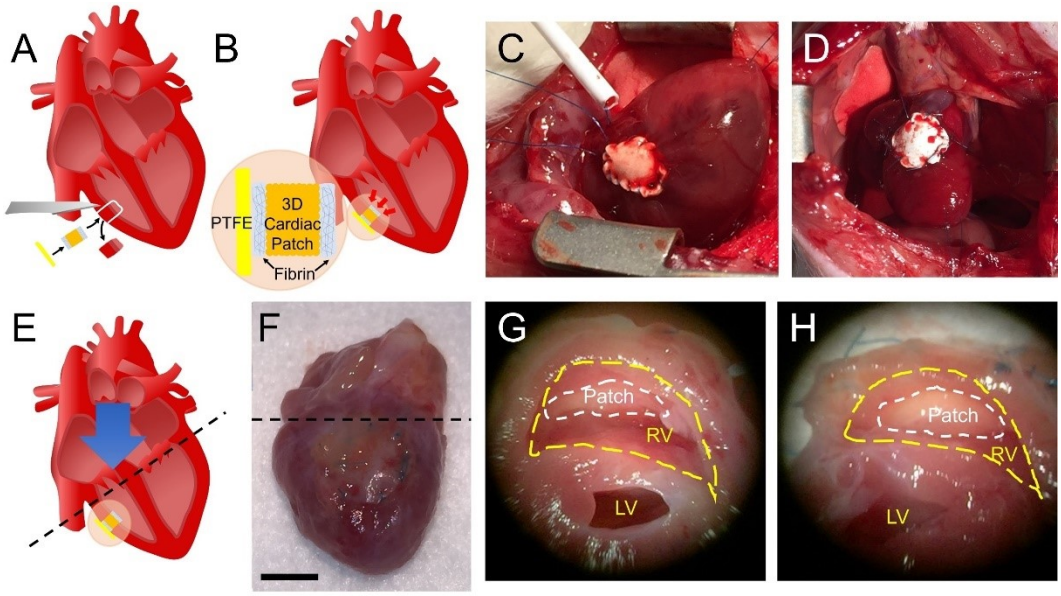

Figure 15: Schematic diagram of *in vivo* transmural 3D cardiac patch implantation. Panels A, B demonstrates the full-thickness heart repair model (C-D), with cross-sectional views (E-H) 1-month post-implantation. The black dotted lines indicate the cut made for the cross-sectional views. The blue arrow indicates the view for cross sectional views G and H, where the 3D cardiac patch is outlined by the white dotted line and the RV is outlined by the yellow dotted line.

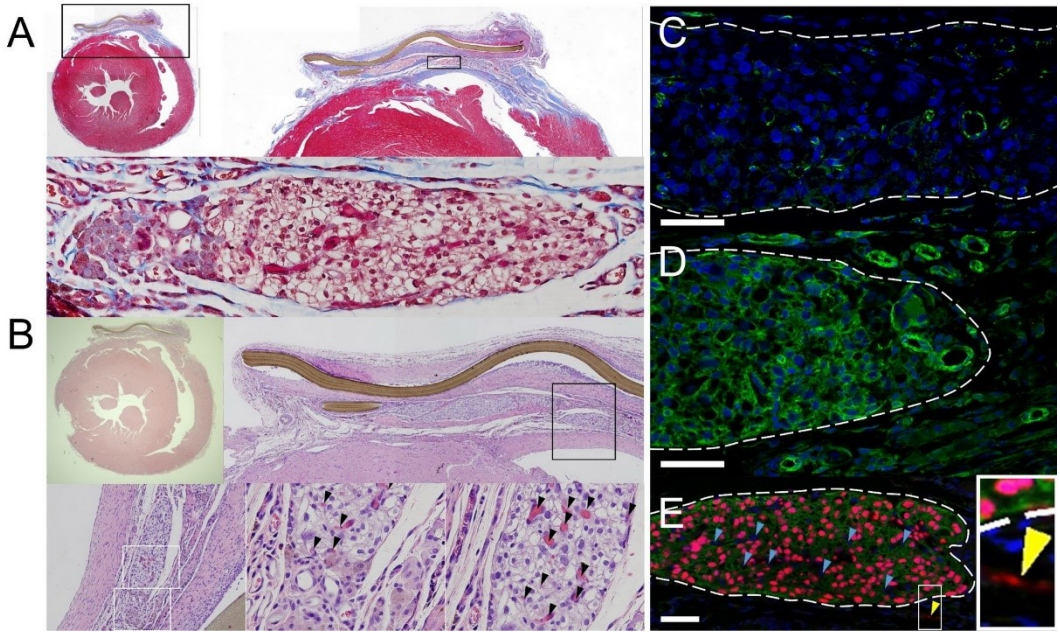

Figure 16: Histology and immunofluorescence of transmural 3D cardiac patch. A-B: Masson Trichrome (A), H&E (B) stains of implanted 3D bioprinted patch. C-E: Immunofluorescence of implanted 3D bioprinted patch. C: Green: CD31, D: Green: Alpha actinin, E: Green: Troponin, Red: Human nuclear antigen (HNA). All: Blue: DAPI. White dotted line indicates the boundaries of implanted 3D bioprinted patch. Yellow arrows indicate HNA+ cells, light blue arrows indicate HNA- DAPI+ rodent cells. Scale bar: 50 μm.

4.5 3D cardiac patch maturation using chemical factors

The use of hiPSC-CMs in translational medicine is hampered by the fact that these cells do not achieve the full functional maturity of an adult cardiomyocyte (69-71). Scientists and tissue engineers have tried to various ways of improving maturation

of hiPSC-CMs, one of which is chemical maturation using defined chemical factors (72). We created 3D bioprinted cardiac patches made of hiPSC-CMs and chemically treated these patches with thyroid hormone, insulin-like growth factor 1 and dexamethasone (TDI). We have used these CMs to create 3D bioprinted patches (Figure 17), and have noted increased sarcomere length (Figure 17A-B), increased conduction velocity (Figure 17C) and a more mature cardiomyocyte transcriptional profile within the 3D bioprinted cardiac patches (Figure 17D-F). There were no significant differences in ejection fraction after *in vivo* implantation and echocardiography at 1 month of TDI-treated cardiac patches, compared to untreated cardiac patches, possibly due to the small size of the implanted cardiac patches, which may be the basis for a future study.

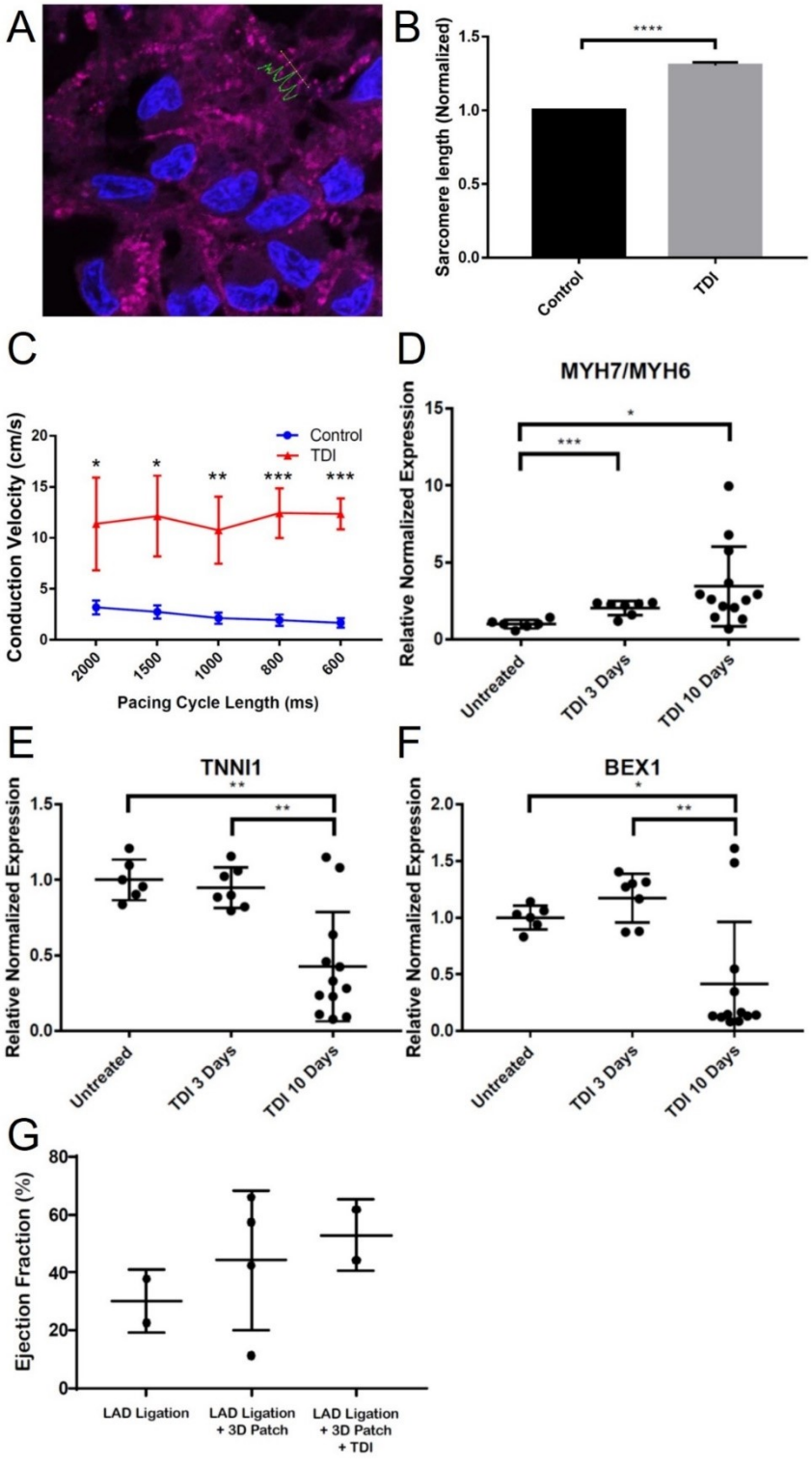
A
B
Sarcomere length (Normalized)
****
Control
TDI
C
Conduction Velocity (cm/s)
Control
TDI
Pacing Cycle Length (ms)
2000
1500
1000
800
600
D
MYH7/MYH6
Relative Normalized Expression
Untreated
TDI 3 Days
TDI 10 Days
E
TNNI1
Relative Normalized Expression
F
BEX1
Relative Normalized Expression
G
Ejection Fraction (%)
LAD Ligation
LAD Ligation + 3D Patch
LAD Ligation + 3D Patch + TDI

Figure 17: Functional changes of 3D bioprinted cardiac patches with TDI treatment. (A) Representative confocal microscopy image of cryosectioned a TDI-treated 3D bioprinted cardiac patch, stained with DAPI (blue) and alpha-actinin (purple) (B) Quantification of sarcomere length in TDI-treated vs untreated 3D bioprinted cardiac patch (**** $p < 0.0001$) (C) TDI treatment improves electrophysiological conduction of 3D bioprinted cardiac patches (* $p \leq 0.05$, ** $p \leq 0.01$, *** $p \leq 0.001$) (D-F) TDI treatment leads to a more mature cardiomyocyte transcriptional profile within the 3D bioprinted cardiac patches (* $p \leq 0.05$, ** $p \leq 0.01$, *** $p \leq 0.001$) (G) In vivo implantation and echocardiography at 1 month.

Chapter 5

Cardiac disease modelling using 3D spheroids and CRISPR interference

5.1. Introduction

Calmodulinopathies, caused by mutations in calmodulin (CaM), a ubiquitous Ca^{2+} sensor, can lead to life-threatening cardiac arrhythmias such as long QT syndrome (LQTS), catecholaminergic polymorphic ventricular tachycardia (CPVT) and idiopathic ventricular fibrillation (IVF) (73, 74). For example, a p.D130G-CaM amino acid substitution, resulting from a heterozygous c.389 A>G single nucleotide substitution in *CALM2*, has been shown to mediate a decrease in Ca^{2+}/CaM-dependent inactivation (CDI) of L-type Ca2+ channels (LTCCs), leading to prolonged action potentials (APs) and a cellular LQTS phenotype (11). As there are 3 CALM genes (*CALM1, CALM2, CALM3*) encoding for the identical CaM protein, selective and efficient silencing of *CALM2* using a variant of CRISPR/Cas9 technology, CRISPR interference (75, 76) (CRISPRi), has been shown to lead a downregulation of mutant CaM expression and functional rescue of the calmodulinopathy phenotype in two-dimensional (2D) monolayers (11).

Meanwhile, three-dimensional (3D) tissue engineering has the potential to overcome roadblocks to 2D cardiac cell therapy by offering enhanced cell survival

and retention, prolonged paracrine release and structural support (77). Engineered *in vitro* 3D models of diseases also enable new insights into disease mechanisms and provide an opportunity to screen new therapies (78) before clinical application. In some circles, this has been termed 'clinical trials 'in a dish' (79). CRISPR/cas9 technology has been used in 3D organoid models (80, 81) but most of this work involves generating reporter cell lines or the introduction of mutations for disease modelling.

Combining 3D tissue engineering with powerful programmable nuclease-based CRISPR/cas9 genome engineering tools provides an opportunity to study and gain further insight into the effects of the added dimensionality as a tissue model of cardiac arrhythmia, to uncover disease mechanisms in 3D, such as during human organ development. This also represents a further step towards making the promising strategy of using CRISPRi for the treatment of congenital LQTS resistant to conventional therapy a clinical reality, without permanent alteration to the genome.

5.2. Materials and Methods

Generation of hiPSC-CMs and 2D monolayers

hiPSC-CMs were generated from a patient with D130G-CALM2-mediated LQTS (11) and differentiated to form cardiomyocytes using standard methods (2, 82)

(Figure 18A-B). The hiPSC-CMs were first replated to form confluent 2D monolayers and then used to make 3D cardiac tissues.

CRISPR interference and lentiviral creation

The cloning of lentiviral constructs and screening of gRNA candidates have been discussed in a previous publication (11). CRISPRi is employed to selectively suppress both wildtype (WT) and mutant *CALM2* expression, thus down-regulating mutant D130G-CaM expression, reducing disrupting of CDI of LTCCs and functionally rescuing the cellular LQTS phenotype. To generate lentiviruses, HEK293T cells were separately transfected (Lipofectamine 2000, Invitrogen) with packaging plasmids, envelope plasmids and transfer plasmid encoding either an enzymatically dead Cas9 fused with suppressor Krüppel-associated box (KRAB), a guide RNA (gRNA) backbone or the gRNA targeting CALM2 (both WT and mutant). Lenti-X-Concentrator (Clontech Laboratories) was then used to concentrate infectious lentiviral vector particles according to the manufacturer's recommendations. 2D and 3D cardiac tissues were then simultaneously transduced with 2 lentiviruses, either KRAB/gRNA-CALM2 or KRAB/gRNA-backbone as control (Fig 1B).

mRNA expression by qualitative PCR (qPCR)

Cardiomyocytes in 2D and 3D preparations were harvested for qPCR quantification to determine CALM1, CALM2 and CALM3 mRNA transcript levels.

Biomaterial-free 3D cardiac spheroid (CS) creation

The detailed method for creating biomaterial-free 3D cardiac spheroids has been discussed in previous papers by our group (2, 82). Briefly, hiPSC-CMs were dissociated and co-cultured with dissociated supporting cells, such as human cardiac fibroblasts (Sciencell, Carlsbad, CA) and/or human umbilical vein endothelial cells (Lonza, Basel, Switzerland), in ultra-low attachment 96-well plates. Within 3 days, they form 3D cardiac spheroids (2, 82).

Biomaterial-free 3D bioprinting

We have also published the method for biomaterial-free 3D bioprinting (19) in previous publications by our group (2, 82). Briefly, CSs were picked up by vacuum suction using a robotic arm and transferred onto a stainless-steel needle array (Cyfuse Biomedical K.K., Tokyo, Japan), where they fuse over another 3 days to form a biomaterial-free 3D bioprinted cardiac patch.

Electrophysiological studies

We have previously described our method for electrophysiological optical mapping (82) and applied the same method to both CSs. Briefly, 2D monolayers (Figure 18A-B, Supplementary Figure A.6), 3D CSs were stained with a voltage sensitive dye di-4-ANEPPS and paced at decreasing pacing cycle length until loss of capture. Optical recordings were obtained at pacing cycle lengths 2000 ms, 1500 ms, 1000 ms and 900 ms for 2D monolayers (Figure 18) and 2000 ms, 1500 ms, 1250ms, 1000 ms, 800 ms, 600 ms and 400 ms (Figure 20) using a 100 × 100 pixel CMOS camera (MiCAM Ultima-L, SciMedia, Costa Mesa, CA) (Figure S6). In addition, CSs were placed in a customized chamber to hold the spheroids in position and prevent movement artifacts.

Microscopy

Optical microscopy images were taken using the EVOS XL CORE imaging system. Immunofluorescent and transmitted monochrome microscopy images and videos were taken using the EVOS FL imaging system. Confocal microscopy images were taken using the Zeiss LSM780 Confocal microscope.

5.3. Results

5.3.1. CRISPRi in 2D

The APD_{80} shortened by 23% (p=0.02) with pacing at 2000 ms and by 17% (p=0.01) at 1500 ms (Figure 18C). There were no statistical differences in APD_{80} at pacing cycle lengths 1000 ms and 900 ms. Additionally, the minimal capture cycle length decreased to 694 ± 31 ms from 1100 ± 167 ms (p=0.04) (Figure 18D). CALM2 mRNA expression decreased significantly to 0.62 ± 0.06 compared to the control ($p < 0.01$), whereas CALM1 expression (1.01 ± 0.07 (p=0.63)) and CALM3 expression (0.98 ± 0.03 (p=0.07)) remained unchanged (Figure 18E).

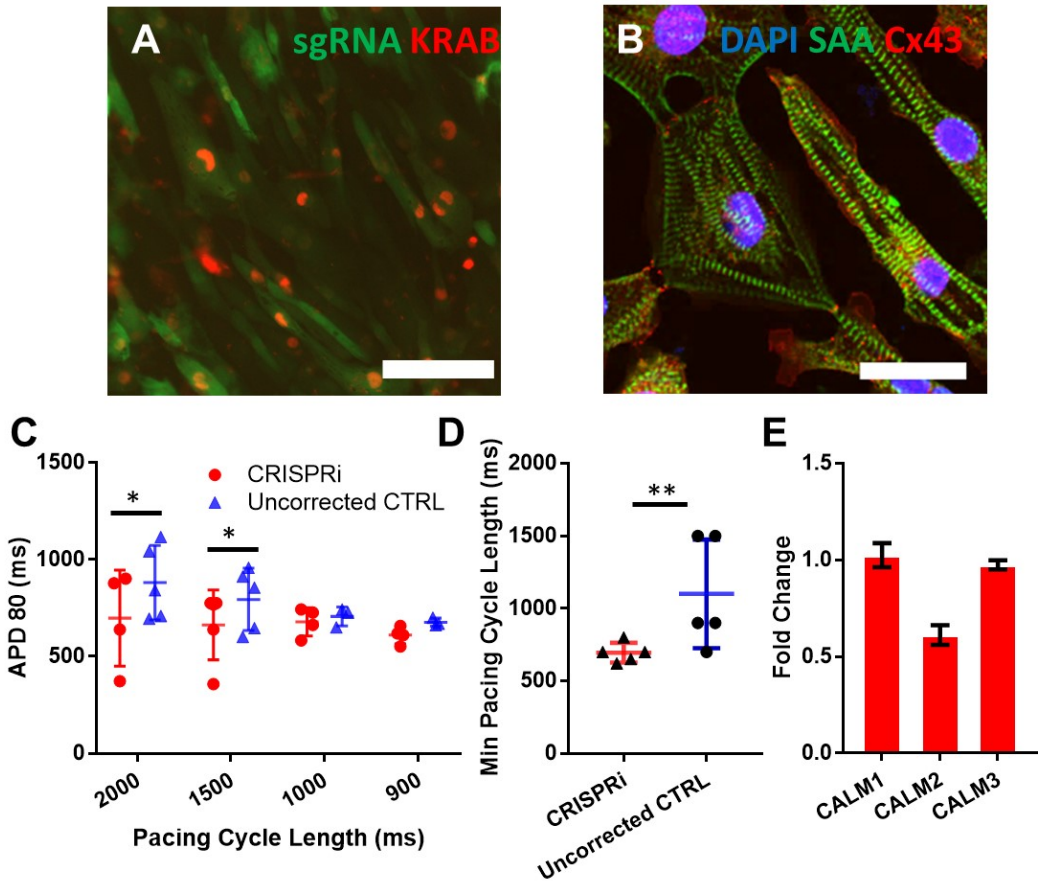

Figure 18: Cellular LQTS phenotype recapitulated in 2D monolayer using CRISPRi. A: D130G-CALM2 2D hiPSC-CM monolayer treated with lentiviruses encoding KRAB transcriptional repressor (red fluorescence) and gRNA-CALM2 (green/cyan fluorescence). Scale bar: 50 µm. B: Confocal microscopy image of a D130G-CALM2 2D hiPSC-CM monolayer (Green: α-Actinin, Red: Cx43, Blue: DAPI). Scale bar: 25 µm. C: APD_{80}. D: Minimum capture cycle length. E: CALM mRNA expression of D130G-CALM2 2D hiPSC-CM monolayers. * indicates p values. *, $p < 0.05$; **, $p < 0.01$; **, $p < 0.001$

5.3.2. 3D Cardiosphere (CS) tissue model of D130G-CALM2-mediated long QT syndrome (LQTS)

We were able to generate 3D CSs using hiPSC-CMs with D130G-CALM2-mediated LQTS (Figure 19A), record optical action potentials (APs) from them (Figure 19B), and use them for biomaterial-free 3D bioprinting (Figure 19C). The CSs fused to form an intact beating 3D cardiac patch (Figure 19D-E), that was amenable to electrophysiological studies (Figure 19F). Optical action potentials were recorded from the 3D cardiac patch (Figure 19G), and demonstrated prolonged APs when compared to 3D cardiac patches made from WT hiPSC-CMs without disease (82), indicative of 3D tissue electrophysiological LQTS phenotype.

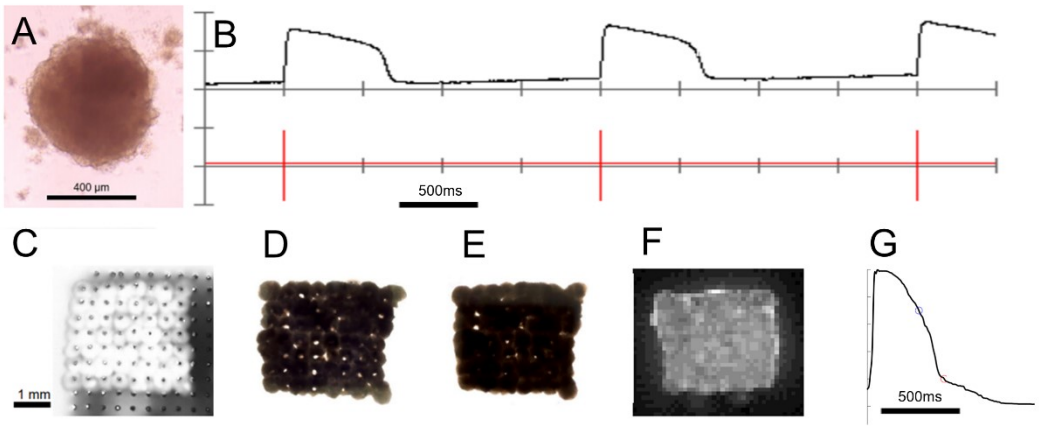

Figure 19: 3D CSs and 3D bioprinted cardiac patches as 3D tissue models of calmodulinopathy. A: 3D CS created using D130G-CALM2 hiPSC-CMs B: Action potentials (black trace) recorded by optical mapping. The stimulation artifact is shown in red (2000 ms pacing CL). Scale bar: 500 ms. C-F: Creation of 3D

bioprinted cardiac patch created using D130G-CALM2 hiPSC-CMs, at the end of 3D bioprinting (C), at decannulation (D), 2 days after decannulation (E), and at electrophysiological optical mapping (F). Scale bar: 1mm. G: Representative optical action potential from a 3D cardiac patch. Scale bar: 500 ms.

After transduction with CRISPRi viruses, the 3D CSs exhibited both red and green fluorescence (Figure 20A-D), indicating that the KRAB transcriptional suppressor and the gRNA were being expressed respectively. CRISPRi shortened action potentials (Figure 20E) without significant reduction in minimum pacing cycle length (Figure 20F). When quantified, the APD_{30} was shortened across all pacing cycle lengths (2000 ms, 1500 ms, 1250 ms, 1000 ms, 800 ms, 600 ms and 400 ms) (Figure 20G) and the APD_{80} was shortened at pacing cycle lengths 2000 ms, 1500 ms and 400 ms (Figure 20H). In addition, we noted a reduction in electrical alternans at longer pacing cycle lengths in the CRISPRi group, indicating better stability of repolarization in the 3D CSs after CRISPRi (Figure 20E).

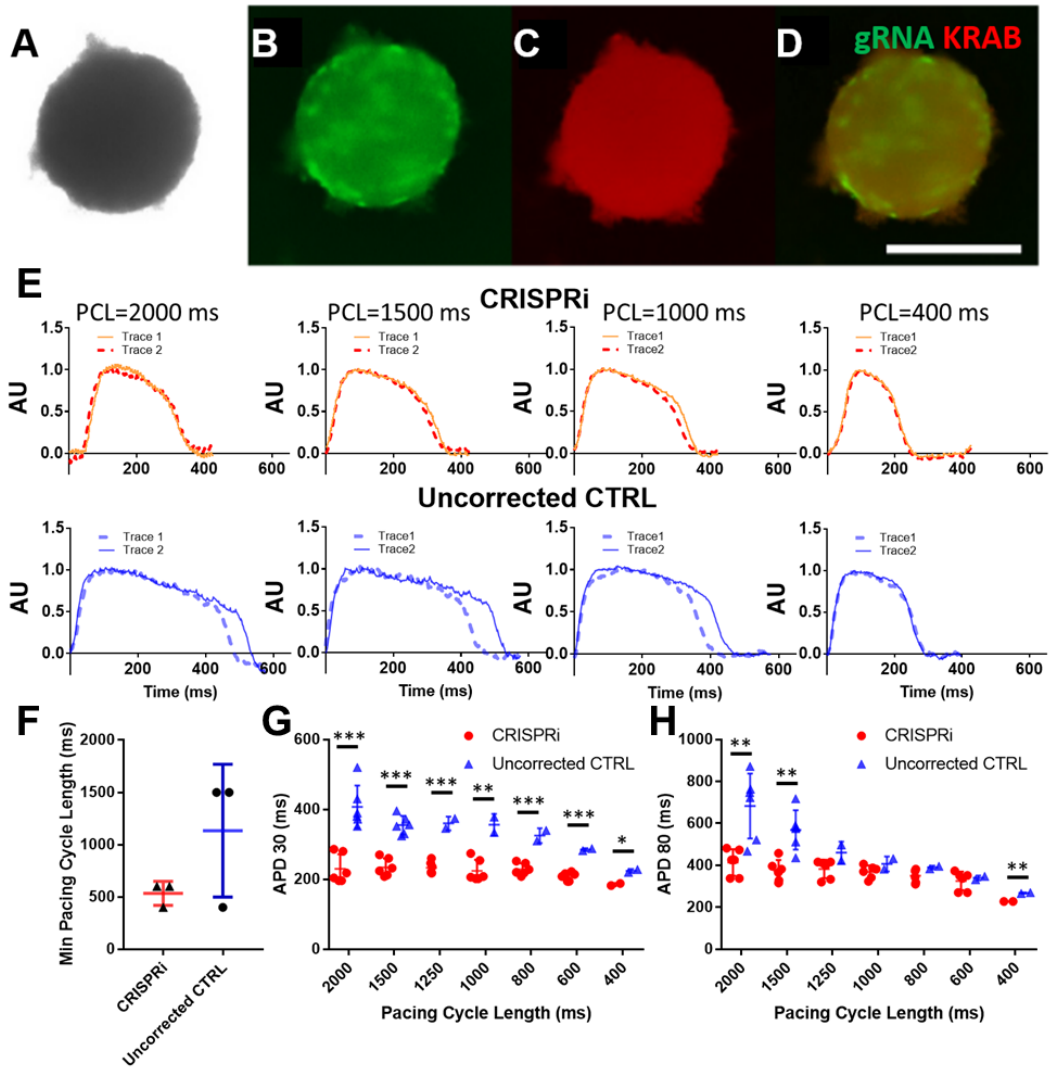

Figure 20: Correction of pathological electrophysiology phenotype in D130G-CALM2 3D CSs using CRISPRi. A-D: 3D CSs were transduced with lentiviruses encoding gRNA-CALM2 (green/cyan fluorescence) and KRAB transcriptional repressor (red fluorescence) (A: Transmitted light B/C/D: Green/Red/Merged fluorescence). E: Representative action potentials (APs) demonstrating shortening of AP and reduction in electrical alternans using CRISPRi. F-H: Minimum pacing

cycle length (F), APD_{30} (G) and APD_{80} (H) of 3D CSs. A single asterisk indicates a p value less than 0.05, double asterisks indicate a p value less than 0.01, triple asterisks indicate a p value less than 0.001.

5.4. Discussion

Most applications of CRISPR in tissue engineering involve correcting mutations in 2D first, as induced pluripotent stem cells, then using CRISPR-corrected cells for tissue engineering (83, 84). While that may be relevant for creating 3D tissue from scratch, conceptually that is not as clinically relevant as performing CRISPR correction in already-formed intact 3D tissues for the purposes of disease modeling. In this present study, to our knowledge, we were the first to demonstrate CRISPRi in 3D cardiac tissue.

A change in electrophysiological phenotype was observed after CRISPRi. 3D cardiac tissue made using mutant hiPSC-CMs recapitulated LQTS and exhibited prolonged optical action potentials (Figure 19) (APD_{30} 255 ms, APD_{80} 444ms), compared to 3D cardiac tissue made from hiPSC-CMs without disease (WT) (APD_{30} 189 ms, APD_{80} 250ms) (82).

These APDs shortened significantly after CRISPRi knockout of mutant CALM2 (Figure 20). CALM2-D130G binds to calmodulin targets, but does not bind Ca^{2+} in

the C-lobe and thus does not produce CDI of LTCCs. The non-inactivating LTCC is associated with the persistent depolarizing current that prolongs the APD. CRISPRi targeting CALM2 knocks down expression of both WT and mutant CaM2, allowing for CaM1 and 3 to compete for binding. These CaMs have retained Ca^{2+} binding, thus mediating CDI of the LTCC, reducing depolarizing current and shortening APD. Thus, CRISPRi in 3D CSs functionally rescues the calmodulinopathy phenotype and ameliorates pathologically prolonged APDs, back to WT.

There are several advantages to using 3D cardiac tissue with an added dimension compared to 2D. CSs can be 3D bioprinted to form 3D patches (Figure 19), which can subsequently be used for disease modeling if larger 3D cardiac tissue is desired. These cardiac patches can also be used for tissue regeneration or creating artificial organs. At the same time, CSs can be used for quality control and high throughput spheroid drug screen (85), as 3D CSs are more similar to the actual heart muscle and thus more clinically relevant, than individual cells in 2D monolayers.

A notable finding is that for CRISPRi to work in 3D tissue, there is no need for 100% transduction to effect a phenotype change. There is also no need for a 100% CALM2 knockdown to effect a phenotype change (Figure 18). This may be due to the fact that the 3D tissue is a well-connected syncytium and once there are a critical

number of CRISPR corrected cells and a critical reduction in existing mutant CALM2, there is a resultant electrophysiological phenotype.

5.5. Conclusions

In this study, 2D cellular LQTS phenotype and 3D tissue LQTS phenotype were recapitulated in 2D monolayers and 3D CSs respectively. CRISPRi successfully corrects pathologically prolonged cardiac APs, reducing APD_{80} and APD_{30}, in different 3D models and we were able to modulate electrical phenotype in both 3D models. The added dimensionality afforded by tissue engineering allows for the generation of larger tissues of customized 3D geometry using 3D bioprinting in the case of CSs, such as 3D bioprinted cardiac patches, and hence the study of correction of congenital LQTS in larger tissues by CRISPRi in 3D. CRISPRi has the potential to correct congenital LQTS clinically without permanent alteration to the human genome.

Chapter 6

3D modeling, 3D virtual reality and applications in cardiovascular medicine

6.1. Introduction

Virtual reality (VR) is broadly defined as a three-dimensional (3D) simulation of the real-world, with the ability for a user to interact directly with the simulation (86, 87). VR integrates imaging data and user input into a unified graphical output, often onto a wearable technology like a headset (86-88). Originally, VR flourished in the gaming community, though its use in medicine dates back to the early 1990s (87). In its earliest applications to biomedicine, VR was largely applied to the behavioral sciences (87), though the advent of "controllers" or sensors that track hand position and movements in real time have vastly expanded the ability to interact with the virtual space and thus its applications to surgery. Presently, VR is widely used in medicine, from stroke rehabilitation (89), to tools for trainees to learn how to perform laparoscopic surgery (87, 90).

This interactive rendered 3D environment of VR lends itself well to diseases involving complex anatomy, such as congenital heart disease (CHD), complicated neurovascular pathology and fetal therapy, as surgical or procedural planning involves careful pre-surgical or pre-procedural discussion of often widely varying

and nuanced structural cardiovascular disease. Planning of surgical patch or baffle placement, conduit sizing, placement of surgical cannulae or approach (in cases of cardiac malposition) can vary by patient. Utility of a 3D modality beyond traditional echocardiographic and cross-sectional imaging is currently underscored by the rise in 3D printing (91-93). In pediatric cardiology and cardiac surgery, the use of VR is emerging. In published literature, VR was used to construct a training tool for minimally invasive surgery (94). However, this method lacked the ability to interact with the heart, nor could it provide interactive sectioning or 4-chamber views.

Beyond surgical planning, VR has also been utilized as a training tool for residents and medical students (87, 90). Simulators can incorporate VR to immerse trainees in a virtual rendering of a range of different procedures, particularly with laparoscopic procedures (87, 90). Previous studies have shown that trainees who use these VR simulators in their surgical curriculum face shorter times to completion of their learning tasks compared to their counterparts who did not use VR (87). The use of VR for surgical planning has been demonstrated in plastic and orthopedic surgery (95) wherein surgeons created VR models of their surgical sites and simulated the planned procedure.

We present 3 novel uses of VR in CHD, neurovascular pathology and fetal medicine, to create virtually rendered high fidelity 3D VR models of the pediatric hearts, complex pseudoaneurysm of the internal carotid artery and fetal hearts respectively, viewed via a VR headset and controller platform for visualization and manipulation.

Additionally, in Section 5 of this chapter, we present a pilot study demonstrating the feasibility of 3D bioprinting patient-specific customized biomaterial-free cardiac tissue with complex shapes and geometries. The same 3D models, described in Sections 2, 3 and 4, and selected parts of the 3D models can be used as the 3D template for 3D bioprinting in Section 5.

6.2. Congenital Heart Disease

In this example, we used high resolution cardiac multidetector computed tomography (CT) source data to reconstruct 3D virtual models from two patients: one with truncus arteriosus type IV with arch anomalies and another with a large ventricular septal defect and congenital diaphragmatic hernia (CDH) causing cardiac malposition; these cases were selected to demonstrate common periprocedural concerns regarding intra- and extracardiac anatomy. The models, controlled in real time by the end user, allow customized and real time immersive viewing. This technique has the potential to aid in the pre-surgical planning of

complex cardiothoracic surgical procedures by assisting in visualization of complex spatial anatomy.

6.2.1. Data acquisition and 3D segmentation

CT of the heart performed following administration of intravenous contrast and was exported using Carestream Vue (Rochester, New York, USA). 3D segmentation was performed using DICOM to Print (D2P) software (3D Systems, Rock Hill, SC) using auto-segmentation and/or thresholding by Hounsfield unit to identify the blood pool. A 3D volumetric mask was first created and processed using cutting and Boolean subtraction tools. Finally, the 3D mask was converted into a 3D surface mesh for VR visualization. Depending on the complexity of the case and the experience of the operator, this 3D segmentation process can take less than 30 minutes, or up to several hours.

6.2.2. VR Visualization

VR visualization was performed at the Johns Hopkins Carnegie 3D Printing and Visualization Facility using a VR platform (Figure 21A), consisting of a VR headset with two controllers (HTC Vive, New Taipei City, Taiwan). An area of 12 feet by 12 feet was designated for VR, and two base stations were used to detect the exact spatial location of the VR user and the two controllers. The 3D segmented mesh (Figure 22) was visualized into VR using D2P software (3D Systems, Rock

Hill, SC). The VR user can magnify, handle and rotate the entire 3D heart model using the left controller (Figure 21B), and section the 3D heart model using the right controller acting as a clipping plane for intracardiac or intraluminal viewing (Figure 21C-E). To examine the sections at various angles, the VR user can either walk around or closer to the 3D heart model visualized in VR, or move, magnify and rotate the object using the left controller. Open Broadcaster Software Studio (Version 20) was used to capture the VR views (Figure 21B-E, Video B.4).

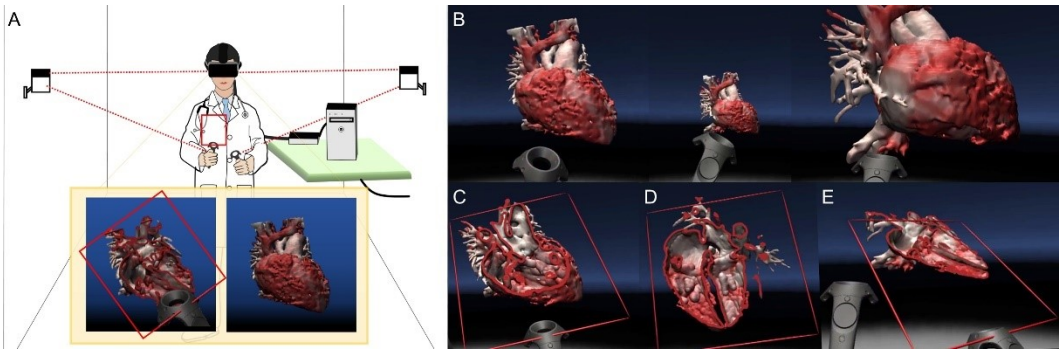

Figure 21: VR visualization of the heart. (A) Schematic diagram demonstrating the VR set-up (B) Various magnifications (C) Persistent Truncus Arteriosus (D-E) Apical 4 chamber view.

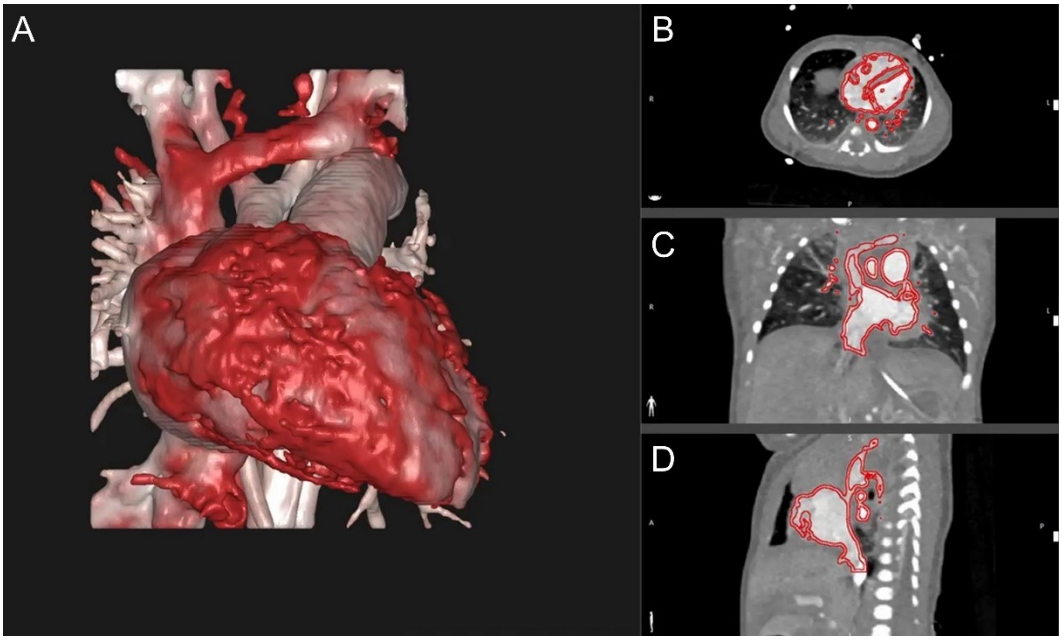

Figure 22: 3D segmentation of the heart. (A) 3D heart model post-segmentation (B) Axial view (C) Coronal view (D) Sagittal view.

6.2.3. Case 1

A 2.95 kg baby girl was delivered at full term with a prenatal diagnosis of truncus arteriosus, ventricular septal defect (VSD) and aortic arch hypoplasia. The initial postnatal echocardiogram on day of life (DOL) 1 demonstrated truncus arteriosus type A4 (Van Praagh classification) with ascending aortic arch hypoplasia with coarctation versus arch interruption. A CT angiogram (CTA) of the chest was performed on DOL 2, confirming the diagnosis of hypoplastic aortic arch without interruption.

The CTA dataset was segmented and processed to create a 3D model which was projected into VR. 3D visualization and dynamic manipulations (Figure 21B), live sectioning of the 3D heart model to view the VSD as well as the hypoplastic aortic arch (Figure 21C-E) was performed successfully in the VR space.

The patient subsequently went to the operating room on the 3rd day of life for complete repair with an aortic arch reconstruction using PA homograft patch, patent ductus arteriosus division, 10 mm RV-PA conduit (femoral vein graft), patch repair of the VSD, and ASD partial closure. The patient made an uneventful recovery. The anatomy was accurately represented in the VR space, with improved visualization of the arch for surgical planning (Video B.4).

6.2.4. Case 2

A 5-month-old, 35-week premature infant with a large VSD and right-sided CDH was transferred from an outside hospital for surgical management following CDH repair and history of extracorporeal membrane oxygenation (ECMO).

Initial transthoracic and transesophageal echocardiograms revealed a large inlet type VSD with anterior extension to the paramembranous septum. CT scan performed for assessment of cardiac malposition and lung fields revealed extreme dextrocardia with rightward rotation in the setting of severe right lung hypoplasia

and left lung hyperinflation. VR model of the patient's anatomy allowed user guided manipulation to envision the VSD margins (including relationships to the great vessels) beyond the planes of traditional imaging (Video B.5). Median sternotomy at the time of surgery revealed an anteriorly located dilated main pulmonary artery with no visualization of the right atrium due to posterior shift. Initial venous cannulation was performed in the main pulmonary artery and then converted to right atrial cannulation following cardiac decompression. After physical leftward rotation of the heart, surgical patch closure of the large VSD via a transatrial approach was performed with no residual defects on follow up imaging. The child tolerated the procedure well, including postoperative weaning of pulmonary antihypertensive medications. The VR model accurately represented surgical findings, including VSD visualization in relation to cardiac shift and rotation as well as outflow tracts.

6.2.5. Discussion

The use of VR to generate accurate, patient-specific heart models for immersive anatomical assessment in a neonate or young infant is feasible. User defined controllers allow for spatial manipulation and segmentation of the heart model in real time, suggesting a vital role as a complement to existing imaging modalities in complex CHD.

The conventional and emerging modalities in cardiothoracic pre-surgical planning are computer-based 3D modeling, computer-aided design (CAD) models, and more recently, 3D printed models (96, 97). We believe that our described method of pre-surgical planning using interactive VR with controllers provides several advantages in the growing paradigms of pre-operative planning.

VR vs. 2D Visualizations of 3D Heart Models (from CT, MRI or 3D Ultrasound)

Modalities such as CT, magnetic resonance imaging (MRI) and 3D ultrasound are increasingly used in CHD for 3D spatial demonstration, however these remain limited by 2D monitor-based visualization of 3D models, limited realism and depth perception, as well as inability for user specific manipulation. In VR, the user can move themselves or move the model, allowing for dynamic inspection of the patient's anatomy for visualization from a "surgeon's perspective" while preserving the perception of a 3D space. The surgeon's understanding is also increased by displaying views with VR that cannot be achieved in the OR such as the proximity to "unseen" surrounding structures. Additionally, the adjustable cutting planes allow for visualization of how surgical tools might interact with the anatomy, aiding preparedness for the procedure.

VR also offers an advantage over the current pre-surgical or interventional planning conference format. Traditionally, imaging for each patient is selected and displayed

by the non-invasive imaging pediatric cardiologist to surgeons, interventionalists, cardiologists, anesthesiologists and other relevant providers, including trainees. By shared viewing and real time manipulation of the anatomy by both the cardiologist and surgeons, a better dialogue and shared mental model may be achieved. This shared viewing experience can also be potentially projected into multiple VR screens, now easily available in mass-market mobile phones with cost-effective Do-it-yourself (DIY) cardboard kits, as a teaching tool, and increasingly affordable mixed reality headsets with higher viewing resolution, for actual operative planning. Data security raises important practical concerns.

VR vs. 3D Printed Heart Models

Like 3D printed heart models, VR technology allows for the physical manipulation of complex anatomy, while offering depth perception and visualization with a binocular field of view. VR does offer some specific advantages over rapid prototyping. Visualization of anatomy is malleable, not limited to a single cutting plane or viewing window on a physical model, since 3D masks and meshes can be edited and re-visualized using VR as often as necessary. Planning and expertise for material support apparatus for fine structures is precluded on a virtual model. Finally, the resolution of the VR heart models is not limited to the capabilities of a printer, unlike 3D printed heart models. Using VR, a model can be used to reconstruct all relevant structures with utmost fidelity, with the added benefit of

being able to be magnified or minimized to a wide range of sizes to the operators' preference. The use of high-resolution source data is critical for both modalities and fastidious attention to accurate segmentation allows reconstruction of all relevant structures. A preclinical translational study has shown that with sufficiently high image resolution initially, images based on VR can be fused with the intraoperative imaging environment with good alignment and may even guide intraoperative interventions (98).VR models control costs and upkeep necessary for 3D printing (99), making VR a cost-effective alternative in the long term. Although VR incurs start-up costs such as the purchase of VR equipment (VR headsets, hardware, software, appropriate viewing monitors, etc.), arguably there are comparable start-up expenditures involved for 3D printing as well, such as start-up costs to purchase 3D printing equipment and materials, or fees to use a 3D printing facility. The actual costs vary widely, depending on the quality of the VR equipment and 3D printing equipment/facility. There are equivalent personnel costs for 3D segmentation by specialized technicians for both 3D printing and VR, as 3D segmentation is common to both technologies. However, after initial costs, VR may reduce costs compared to 3D printing, as there is no need to regularly purchase 3D printing material or incur costs pay to use a 3D printing facility. Also, magnification in VR allows for clearer visualization of internal and external structures, which may be otherwise expensive to print. Proper storage and disposal of 3D printed models is of growing relevance, and VR models may provide a more environmentally and

fiscally sustainable form of pre-surgical planning. While digital imaging and communications in medicine (DICOM) storage of VR models is not an insignificant concern, it also offers the advantage of inclusion into the patient's medical record for future reference as well.

Limitations

Use of our software for VR relies on CT, MRI or cone beam computed tomography (CBCT) data to construct the VR model. Echocardiography, the standard imaging modality used for pediatric patients, was not used for VR, however this may be an emerging technology. The incremental use of 3D echocardiography in congenital heart disease and its burgeoning application to 3D printing (100-102) will likely extend to VR as well. Current limitations to the use of 3D echocardiography for rapid prototyping are the lack of standardized image acquisition protocols, and variability in image processing software capabilities and optimization of the 3D dataset, for accurate and convenient segmentation.

An alternative workflow solution is use of a third-party product that allows for accurate STL generation from source 3D echocardiographic data for importing of STL models for VR interaction. Also, upgraded 3D echocardiography machines and updated 3D echocardiography software may potentially allow for the export of 3D STL models directly. The lack of high-resolution data such as CT or MR may

provide a limitation to the use of VR for pre-surgical planning in some pediatric cases. However, when imaging is available, whether in adult or pediatric cardiothoracic cases, VR may contribute potently to pre-surgical planning.

In addition, while VR may be relatively cheaper for multiple 3D segmentations and multiple VR 3D visualizations, a single 3D printed model offers the convenience of portability, without the need for a headset and other specialized equipment. This is important if the model will be referred to in the OR setting. While video recordings of VR (Videos B.4, B.5) can also be conveniently saved and projected onto existing OR computer screens with relative ease, the interactivity with the model is lost in pre-recorded videos. A 3D print can be shared for device planning as well. Other limitations include VR equipment and software start-up costs, the lack of existing standards and insufficient evidence so far to support value (the latter two may reflect the limitations of new technology in general). Ultimately, some products allow a shared workflow for DICOM segmentation of both visualization techniques and use of VR may complement the application of 3D printing.

6.3. Vascular Disease

In this example, we use the same novel VR visualization system for vascular neuroradiology and neurointervention that is designed to enhance the interventional

management of aneurysms. This system has been developed as an adjunct to standard 2D representations.

6.3.1. Data acquisition

A 3D time-of-flight MR angiogram was acquired through the cervical arteries followed by a 3D long axis high-resolution proton density (PD) weighted black blood MRI sequence. After a precontrast mask sequence was acquired, 0.1 mmol per kilogram of a gadolinium-based contrast agent was administered and a 3D contrast-enhanced MR angiogram was acquired during arterial and venous phases. 3D and long and short axis 2D high-resolution black blood MRI sequences were acquired postcontrast, including high-resolution 3D black blood MRI images in coronal and sagittal orientations with T1-weighting. Maximum-intensity projection (MIP) images were reconstructed from the MRA data sets.

6.3.2. 3D Segmentation and Interactive Virtual Reality System

Similar to the previous section, the Digital Imaging and Communications in Medicine (DICOM) dataset was imported into DICOM to Print (D2P) software (3D Systems, Rock Hill, SC) with automatic segmentation and vascular segmentation modules, which were used to identify bilateral carotid vasculature (Figure 23A-C) from their origins in the aorta, to create a preliminary 3D mask. Of note, this is not CT dataset, but rather an MR dataset. Additional processing was performed by

careful review of individual slices to identify smaller vessels and to remove structures that were not of interest. A 3D mesh with opaque (Figure 23D) and translucent views (Figure 23E) was created from the 3D mask. The same VR system (HTC Vive, New Taipei City, Taiwan) was used by neurointerventionalists (Figure 21A, Figure 23F, Video B.6) to visualize and interact with a 3D model of the right carotid pseudoaneurysm in VR. Two base stations were installed to detect the location of the operator wearing the VR headset, as well as the two accompanying VR handheld controllers. The 3D mesh (Figure 23D) was then displayed inside the VR headset (Figure 23G) using D2P software (3D Systems, Rock Hill, SC). One of the handheld controllers was designated for rotation, magnification and handling of the model, and another was designated to act as a clipping plane (Figure 23H) to examine cross-sectional views of the right carotid pseudoaneurysm. For visualization, the operator had the option to move himself or herself physically relative to the displayed object or move the position of the 3D model using the controllers. Two board certified neuroradiologists, with 11 and 6 years of neuroimaging interpretation experience respectively, used the VR projection system to evaluate MRI images of a complex pseudoaneurysm of the right internal carotid artery. Both operators filled in a questionnaire detailing their preferences and observations from this experience.

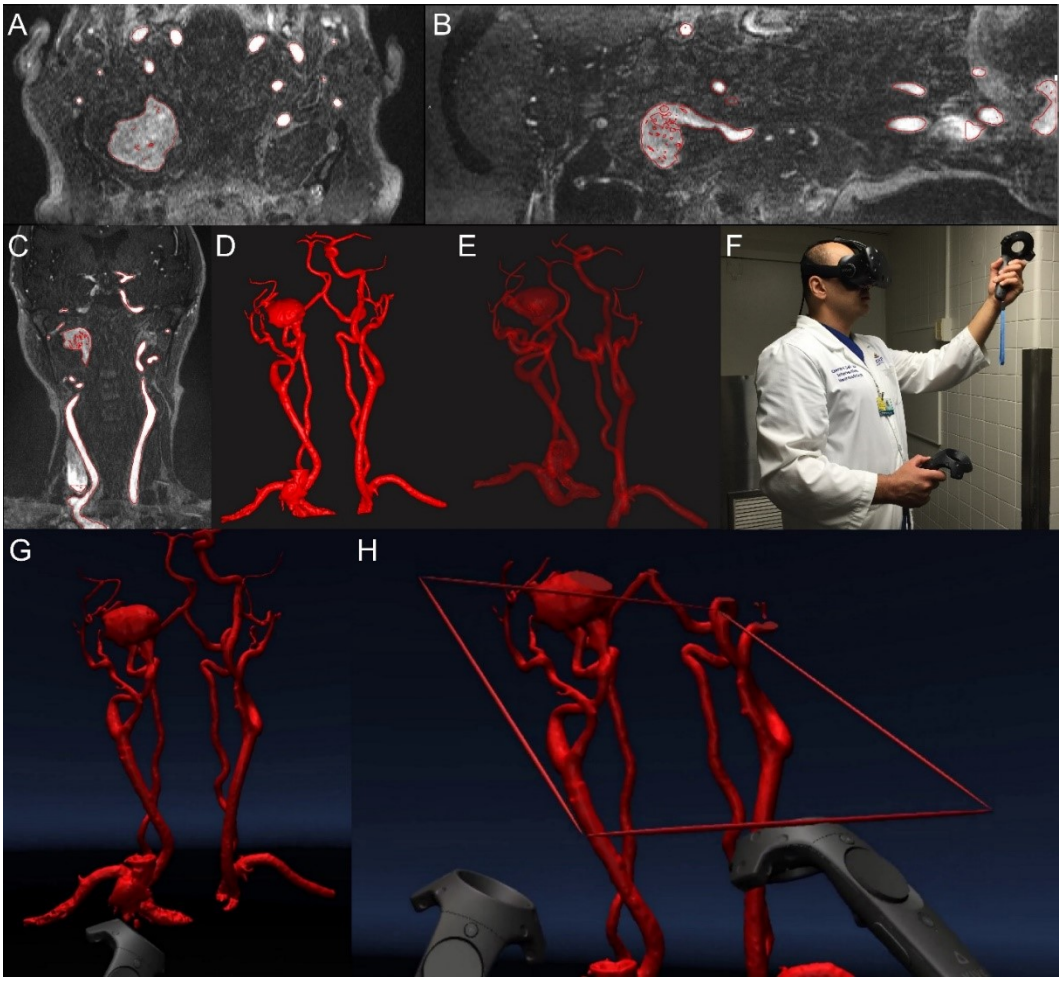

Figure 23: VR projection of right carotid pseudoaneurysm: (A) Axial view, (B) Sagittal view, (C) Coronal view, (D) Opaque view, (E) Translucent view, (F) Interventional neuroradiologist using VR, (G) VR projection, (H) VR projection with realtime sectioning

6.3.3. Results

The segmented DICOM files from 3D angiographic imaging data was successfully loaded into the D2P software VR module and an evaluation was successfully performed in the VR environment.

MRA demonstrated a complex, partially thrombosed, large pseudoaneurysm involving the mid to distal right cervical ICA. The proximal ICA supplying the pseudoaneurysm was moderately to severely narrowed as it was compressed by thrombus at the level of the right lateral mass of C2. The lumen subsequently expanded within the thrombus, filling the inferior aspect of the pseudoaneurysm. There was moderate to severe flattening of the ICA after it exited the pseudoaneurysm with the vessel compressed up against the right mastoid process by the pseudoaneurysm below.

Visualization Modes:

Currently angiographic 3D mesh data could be visualized as both opaque ((Figure 23D) and translucent (Figure 23E) representations, however, only the opaque projection could be seen in VR.

Opaque display: This mode was especially useful when evaluating surface morphological parameters such as lobulations, daughter sacs, and surface irregularities.

Translucent projection: This mode proved particularly helpful to evaluate inflow and outflow tracts and visualize the relationship between overlapping vascular structures.

Visual Landmarks:

Key anatomical landmarks were reliably visualized using both conventional opaque and translucent projection modes (Figure 23A-E) and the virtual environment (Figure 23G-H). The operators were able to visualize outflow and inflow tracts and rotate the model to obtain a working view that clearly outlined a potential trajectory for endovascular device deployment.

Aneurysm size, shape, contour and morphology were all adequately assessed with all details defined on conventional imaging resolved in the VR environment. As more potential views of the aneurysm could be assessed, there were a greater number of potential options for evaluation of size, shape and volume. A true aneurysm volume could be defined (as opposed to an inferred volume based on 2D rendering). Surface morphological parameters, such as of lobulations, daughter

sacs, and surface irregularities were all apparent to the operator. The level of granularity of assessment was at least as high as any depiction on conventional surface rendered radiographic imaging.

Procedural duration:

The operators were both able to complete an entire pre-procedural radiographic work-up in under 10 minutes, including a period of approximately 3 minutes to learn to operate the head mounted VR display and the hand controllers.

Operator preferences and observations:

There was a relatively short learning curve in becoming familiar with the device's controls, getting used to the presence of the VR headset and controllers and being inside the virtual environment. After an adjustment period, the operators found the VR headset and controllers unobtrusive and were able to wear them throughout the procedure without discomfort. The operator did not report any nausea, vertigo or disorientation during or after using the VR device.

6.3.4. Discussion

The past decade has seen a concurrent increase in the use of advanced radiological imaging technologies and minimally invasive intervention in the clinical setting (103, 104). Thus far, understanding 3D anatomical relationships has relied on

visualization of 3D data representations on a flat panel screen. This case demonstrates that current 3D visualization technology allows us to move beyond traditional radiographic monitors to an interactive 3D virtual reality (VR) experience with multiple advantages for patient care, clinical training and medical education.

With VR visualization, the clinician is able to literally immerse themselves into the patient's anatomy and can garner an unprecedented real-time understanding of micro- and macro-anatomy. In the case of the large pseudoaneurysm illustrated in this report, the operators were able to visualize vascular inflow and outflow tracts optimally, as well as infer areas which represented intra-lesional thrombus. This allows for better pre-procedural planning and consideration of various interventional options, including reconstructive options such as placement of stents, or deconstructive options such as vessel sacrifice.

The operators were particularly impressed by the level of detail that could be defined about surface morphological parameters, such as of lobulations, daughter sacs, and surface irregularities, especially since aneurysm wall irregularity and daughter sacs have long been associated with greater risk of sac rupture (105-109).

The operators found the system intuitive (as demonstrated by the short time period required to learn to operate the system). They were also able to quickly adapt to the idea of being immersed in the displayed environment. The VR system uses a high definition display with precise low-latency constellation head tracking capabilities and relies on natural sensorimotor contingencies to perceive interaction with realistic anatomy. The virtual controllers are also of the same dimensions and shape in the virtual environment, resulting in two identical familiar objects in the virtual environment for the operators to quickly adapt to. The operator is able to visualize structures from multiple viewpoints within any portion of the room by moving their own body in a set of instinctively intuitive ways – they can turn their head, move their eyes, bend down, look under, look over and look around to study the object from any angle.

The operator is also provided with a realistic representation of the handheld controller interface with a six degrees-of-freedom and can therefore perform movements (such as picking up virtual objects) that are more intuitive than using a keyboard or mouse. This ability to orient the virtual object in any plane and place it in the visual field using handheld controllers allows the operator to mimic potential patient positioning for surgery or intervention. The observer can reach out, touch, push, pull and perform these or a subset of these actions simultaneously to fully interpret the patient anatomy. This facility may also be helpful in evaluating

images acquired in one position and interpreted in another (such as evaluating anatomic structures in a simulated erect position where the images may have been acquired supine or prone). Preliminary results of the use of this technology suggest a high level of user comfort, ease of use and adaptation to these types of hand-held controllers (110). Through these mechanisms, VR is able to provide an experience that gives rise to an illusory sense of place ("place illusion") and an illusory sense of reality ("plausibility") (111, 112).

In addition to object navigation and orientation, the operator can also utilize one of the controllers as a cutting plane to remove extraneous information from the field of view. This cutting plane is again more intuitive and easier to use than software applications in traditional radiology software visualization packages. Such packages often require technical knowledge in order to crop images and are often cumbersome, requiring multiple steps icons and other user interface shortcuts. The HTC Vive has a controller for increasing or reducing the size of images, which can easily be manipulated, with the use of the operator's thumb. This can therefore be achieved without having to distract from any of the other tasks the operator may be performing (such as cropping the image).

The literature has reported that observers uniformly remark on the realism of the resulting images of VR technology (112, 113). VR has the advantage over

conventional display screens in that it reproduces the way in which light rays hit each eye (114). This has the effect of bringing the virtual object much closer to the operator's eyes and rendering it in a more detailed fashion than would be feasible in a typical diagnostic radiology setting. VR can assist radiological evaluation by considerably diminishing or cancelling out the effects of unsuitable ambient conditions. The viewer is shielded from the outside environment, limiting or removing the effects of suboptimal background lighting, reflective glare, reducing visual distractions and focusing on the subject matter at hand (115).

Beyond the patient care setting, VR technology enables the demonstration of 3D anatomic relationships efficiently and clearly and its use for such educational purposes is expected to increase considerably in the coming years. In an academic conference and peer-teaching setting, VR allows interactive presentations of anatomy and real-time demonstrations to colleagues much like performing an open neurosurgical procedure (without the requirement for the trainee to be in the interventional suite).

There are many potential future directions of applications of VR visualization to vascular neuroradiology and neurointervention that are being explored. Our group is currently working on integrating vessel wall imaging information into a virtual environment using a dataset from Black Blood MRI. Additionally, advances in

segmentation and co-registration may facilitate merging multiple imaging modalities (such as MRI, CT and Nuclear medicine studies) to create a composite virtual object that can detail optimal information about multiple tissues and anatomic structures. Such advances may also allow for the creation of virtual objects representing endovascular devices, which could be sized in a virtual environment prior to being used in a procedure. This would allow the operator to compare the potential merits of different device constructs in an individual case.

6.4. Fetal Therapy

Fetal congenital abnormalities, of which cardiac abnormalities contribute up to 50 percent, is the leading cause of infant death (116-118). Thus, early detection of cardiac abnormalities is crucial since they often require complex surgeries and thus referral to tertiary care centers that can improve the chance of survival for babies with serious heart defects (119). Detection of these cardiac abnormalities can be done through a variety of methods, including fetal cardiac ultrasound between 18 and 22 weeks. Transvaginal scan can also be performed earlier, and fetal echocardiography can be performed in high-risk cases such as with hydrops (120, 121). The detection of fetal abnormalities can alter the pregnancy plan, including planning for therapy, mode of delivery, referral for surgery, or termination (122). Therefore, further technology to enhance the ability to detect fetal cardiac

abnormalities will be beneficial to improve outcomes, preparation, and interventions after birth.

Several of these fetal cardiac abnormalities are critically in need of timely intrauterine intervention to promote survival. Currently, candidates for these interventions are limited, but include aortic valve stenosis with evolving hypoplastic left heart syndrome and a fetal heart block (123). In fact, a study showed that surgery after prenatal diagnosis of hypoplastic left heart syndrome improved survival compared to patients diagnosed after birth (124). Current limiting factors for the development of new interventions are technological challenges and poor candidate selection. There is a need for a guideline for standardized diagnosis of fetal congenital heart diseases and for a multidisciplinary team for interventional diagnosis (125). Thus, the introduction of VR to visualize models of the heart in a virtual 3D space can offer significant advantages in this area.

VR in medicine and its capability to produce an interactive environment with the ability to control objects in an immersive environment (126) can have beneficial effects in visualizing fetal congenital abnormalities and preparing for *in utero* interventions. This example assesses the feasibility of visualizing and manipulating

with 3D models of abnormal and normal fetal hearts derived from 3D ultrasound data.

6.4.1. Methods

We have discussed our system of segmenting 2D computed tomography (CT) or magnetic resonance imaging (MRI) image data to produce 3D models, which are then projected into VR, in previous sections (8, 9). As CT scans are contraindicated in pregnancy and MRI does not have the necessary temporal resolution for acquisition of image data suitable for 3D segmentation, we opted to use 3D ultrasound data. The first step to obtain data using 3D ultrasounds is to define the region of interest and acquire the details of the cardiac anatomy. At the same time, optimize the setting and the imaging window to get the best resolution image and to avoid any artifacts. In our study, the 3D ultrasound volumes of a normal fetal heart and a fetus with right-sided aortic arch were acquired, post-processed and exported as 3D models during cardiac systole. These virtual files were then imported into a VR setup (DICOM to PRINT, 3D Systems, Rock Hill, SC) with controller-based interactive capability (Vive, HTC, Taipei). Two board certified fetal surgeons (AB, JM) and a fetal therapy fellow (MF) tested the VR system and qualitatively assessed the use of this novel technology in fetal therapy.

6.4.2. Results

3D ultrasound data was successfully converted into 3D models of the fetal heart. In VR, these models can be dynamically manipulated in any size in VR as desired by the operator, using VR controllers. The handling and movement of 3D models in VR is akin to that of 3D objects in reality, with high visual resolution afforded by the VR headset similar to 3D objects in reality. The 3D cardiac VR models can be sectioned at different angles to allow the identification of fetal structures (Figure 24). The angles of sectioning are not limited to the typical x-y-z Cartesian planes as seen in traditional 2D visualizations.

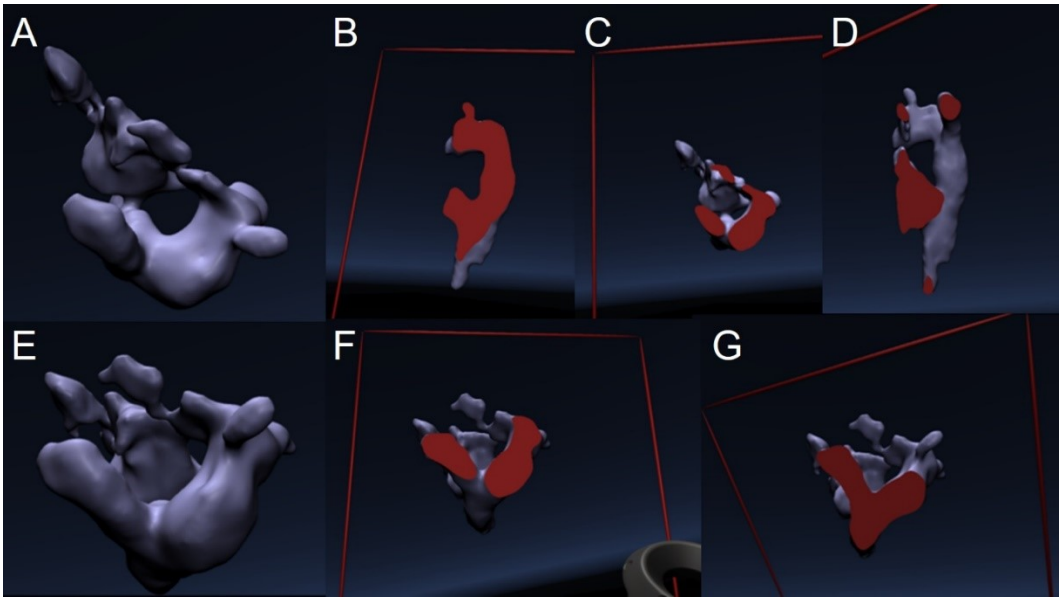

Figure 24: A-D: Normal fetal aortic arch (A) with cross-sectional views (B-D). E-G: Right sided fetal aortic arch (E) with cross-sectional views (F-G).

6.4.3. Discussion

In this study, 3D models were derived from 3D ultrasound volumes of the fetal heart. The advantage of this approach is that the user can manipulate and handle the heart models in virtual space easily. Not only that, the VR models of the fetal hearts can also be sectioned at all angles, which cannot be accomplished in 2D visualizations often presented by other imaging models. VR offers the advantage of performing real-time sectioning and allows unlimited magnification, which is not possible with 3D prints, while reducing material costs associated with 3D printing.

Over the past decade, researchers have adopted VR for a variety of medical purposes, including behavioral treatment for specific phobias (127) and for stroke rehabilitation (128). VR is especially useful for these situations since it provides an opportunity for patients to immerse in new treatments and therapy tasks that cannot be provided in a clinical setting or are often more enjoyable than ones in a clinic (128). For the application of fetal heart imaging, the 3D manipulation capabilities distinguish VR from its imaging counterparts, which are restricted to visualizing an object on the computer screen and often in 2D. There are also many mobile applications that allow users to visualize digitized models of the heart, but these are generally not personalized models of the heart, and they also have limited manipulation, limited to using thumbs and fingers on a small screen or on a physical

screen with limited dimensions using mouse clicks. VR allows operators the ability to manipulate objects with their own two hands, and thus with greater dexterity.

VR can be useful for detecting anomalies and educating patients. There are currently a variety of ways to image the fetal heart during pregnancy, and these are often capable of detecting congenital heart defects *in utero*. Fetal echocardiography can detect most cardiac defects and is a routine antenatal screening method (129). On the other hand, ultrasonography is an imaging modality that is low in cost, high in safety and patient comfort and experience. Fetal MRI is helpful to define a prognosis for fetal central nervous system anomalies (129). VR provide an additional modality for operators to visualize CHDs that can supplement current methods to detect and diagnose CHDs. However, unlike the other methods, VR provides a patient-friendly viewing experience that is easier to understand; it would be easier for operators to explain and educate patients using a 3D reconstruction of their child's heart.

Furthermore, VR can enhance the current technologies available for presurgical planning. One problem in the status quo is that there is a high number of medical errors attributed to limited training and planning opportunities and having rich 3D models of hearts would allow medical professionals to train and prepare for their procedures. Given, the new skills required for minimally invasive surgery and

interventional cardiology, it is important to develop new methods to enhance our ability to perform these methods (130). For example, VR can be used to identify lesions or be used as a method for simulated training. Similar to how VR has been studied to assist with presurgical planning for cerebral gliomas, hepatic surgery, orthognathic surgery or minimally invasive neurosurgery (131-135), this new technology allows for presurgical planning *in utero*.

Despite the many advantages of VR in visualizing the fetal heart, there are several limitations to using VR. One main limitation is the cost involved in setting up such a system, as it involves the initial purchase and setup of expensive computer equipment and headwear required to visualize the images. The additional labor cost of segmentation and rental of equipment for patient use can be a burden for patients who would benefit from this technology, both in terms of cost and ease of use. Furthermore, at this time, these VR projections are not portable as the headset has to be connected to a computer central processing unit (CPU), which may be problematic for settings in the clinic and operating room where individuals may want to easily communicate and transfer VR images. We are aware of attempts to miniaturize VR, driven mainly by computer gamers, so that the CPU is housed in a backpack with a battery pack, which may eliminate this problem in the foreseeable future. Also, at this time, only one person can view and handle the VR object. It is possible to duplicate this projection to another screen for additional viewers to see,

but that corresponding video projection (Video B.7) will not have the VR effect as experienced by the operator handling the object. It may be possible to duplicate the VR projection onto another VR headset, but current technology does not allow for different users to manipulate the same object at the same time, unlike in reality, where a 3D printed object can be passed around and viewed at the same time from different angles by different operators. This is because viewing and using VR is restricted to headsets and corresponding videos.

6.5. Complex 3D bioprinted cardiac tissue

In this section, we demonstrate the feasibility of 3D bioprinting complex cardiac tissue. Firstly, the complex 3D design (Figure 25A) is broken down into multiple 2D slices (Figure 25B-D), and bioprinted by assembling spheroids on a needle array (Figure 25E-I). The complex 3D bioprinted cardiac tissue is then transferred into cell media for further cell culture (Figure 25J-K). After 3 days, the spheroids fuse (Figure 25L) to form an intact tissue that is decannulated and removed from the needle array (Figure 25M-N).

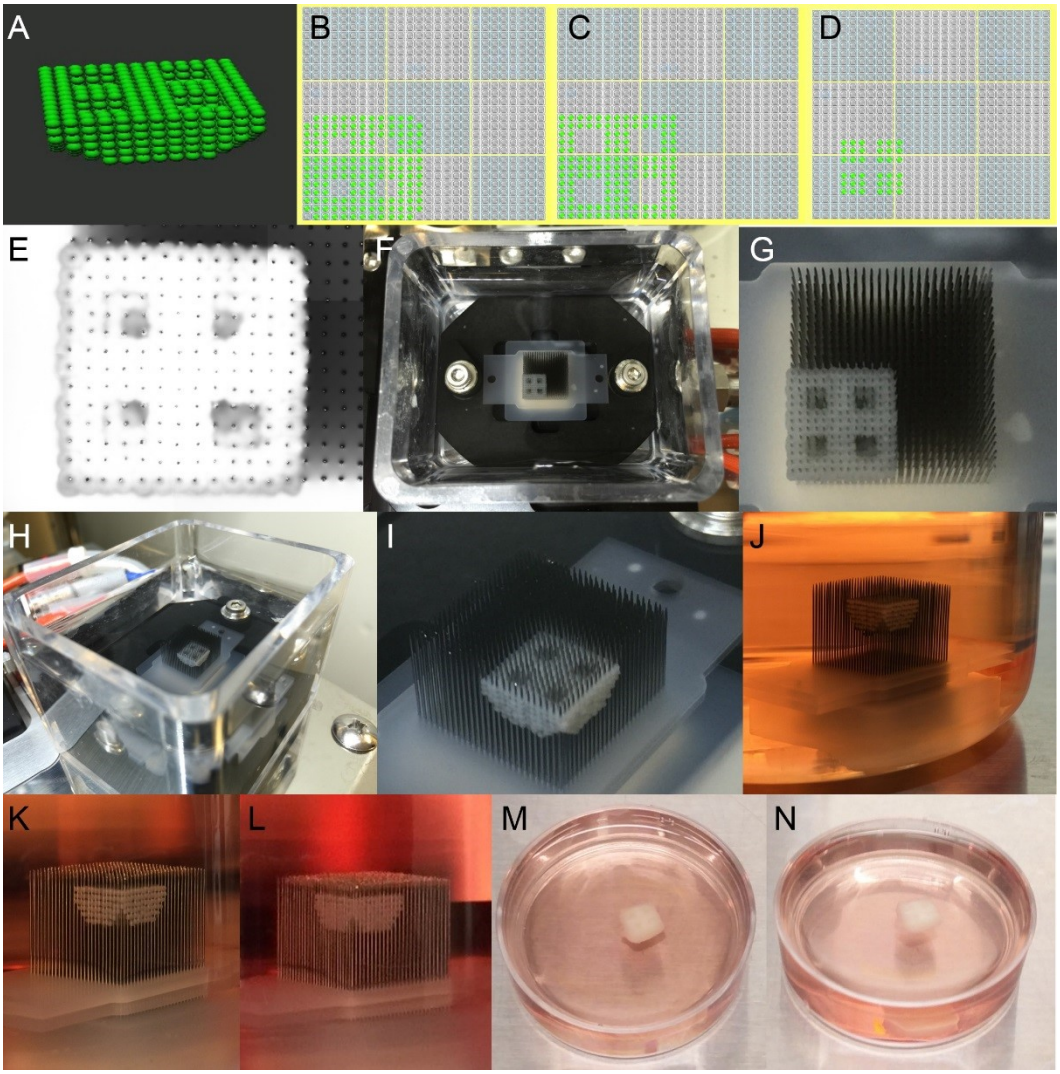

Figure 25: A: 3D design for intended 3D bioprint. B-D: Representative 2D slices of the intended 3D bioprint. E: Complex 3D bioprinted cardiac tissue. F-I: Aerial view of complex 3D bioprinted cardiac tissue, inset (G, I). J-K: Side view of complex 3D bioprinted cardiac tissue after transfer into appropriate cell media. L: Side view of complex 3D bioprinted cardiac tissue 3 days after cell culture. M-N: Macrographs of complex 3D bioprinted cardiac tissue after decannulation.

6.6. Conclusions

We present our preliminary use of virtual reality in cases of CHD, neurovascular pathology and fetal medicine to illustrate the feasibility and potential advantages of this new technology, as well as a pilot study demonstrating the feasibility of 3D bioprinting patient-specific customized biomaterial-free cardiac tissue (a patient-specific 3D cardiac model or part of a 3D cardiac model) with complex shapes and geometries.

In the case of CHD, the selected cases demonstrate complex intra and extracardiac spatial relationships commonly encountered in structural heart disease and were accurate representations of intraoperative findings. Specific advantages of VR in complex CHD include: 1. An immersive environment preserving 3D viewing similar to the operative environment; 2. Customizable visualization in any arbitrary plane by the end user in a preserved 3D viewing space; 3. Cost containment and storage over 3D physical prints, in some cases. Shared viewership may provide the additional important benefit of enhanced trainee education and improved communication amongst providers. While we have represented our use of this technology on two infants, application of VR naturally extends to the growing population of adult congenital patients with complex, sometimes traditional surgical repairs of previous eras, and need for future interventions. For both infants and older patients, the models also facilitate discussion of anatomy and planned

interventions as well as expected outcomes in a tangible format. Future studies are necessary to assess the impact on surgical decision making, training and cost containment.

In the case of neurovascular pathology, we demonstrate the feasibility of using VR as an adjunct to conventional imaging technologies and physical displays for the pre-therapeutic evaluation of neurovascular pathology. This novel visualization approach may represent a valuable adjunct tool for neurovascular pathology in general, notably when subtle nuances in aneurysm morphology and angio-architecture are critical for therapeutic decision making.

In the cases of fetal medicine, we present a novel use of VR for the interactive visualization of normal and abnormal fetal cardiac anatomy, using prenatal 3D ultrasound data. Advantages of this system include the ability to easily visualize a fetal heart with unlimited magnification and from unlimited angles, compared to other imaging modalities of the fetal heart, as well as to provide an assistance tool for presurgical planning. However, several limitations need to be addressed including the limited image sharing capabilities. We expect that future developments, both in the medical field and elsewhere, will continue to address these concerns, and this technology will deliver widespread value to patients.

Chapter 7

Executive summary, Conclusions

7.1. Executive Summary

In this PhD thesis dissertation:

- We demonstrated biomaterial-free methods to create patient-specific 3D cardiac spheroids and 3D bioprinted cardiac patches using hiPSC-CMs.
- The 3D bioprinted cardiac tissue demonstrate mechanical and electrical integration of component cardiac spheroids, with spontaneous beating *in vitro*.
- 3D bioprinted cardiac tissue demonstrate promising *in vivo* biological function when implanted in rodent models.
- Biomaterial-free cardiac tissue made using hiPSC-CMs generated from a patient with an inherited calmodulinopathy, resulting in congenital long QT syndrome, recapitulate disease phenotype with prolonged cardiac action potentials
- CRISPR interference successfully corrects this disease phenotype, shortening the prolonged cardiac action potentials significantly.
- 3D models of cardiovascular structures can be projected into interactive VR for visualization and presurgical/preprocedural planning.

- Biomaterial-free 3D bioprinting can be used for complex 3D designs, including multilayered structures.

7.2. Broader Lessons

The dissertation demonstrates the feasibility of biomaterial-free 3D bioprinting in the field of cardiology and cardiac surgery. It demonstrates the uses of biomaterial-free 3D cardiac tissue for cardiac regeneration and cardiac disease modelling. It also shows how complex patient-specific anatomy can be converted into 3D model, and projected into interactive VR for congenital heart disease, neurovascular pathology and fetal medicine. These complex patient-specific anatomical structures can be 3D bioprinted without biomaterial.

7.3. Future Work

Future work can focus on, extending the *in vivo* application of these cardiac tissues to larger animal models, e.g. sheep, pig, dog, to gather more preclinical data. CRISPR interference can be used to correct other diseases other than the CALM2 mutation demonstrated in this study. CRISPR correction may also be performed instead. VR can also be used prospectively in clinical trials to improve patient care.

Supplementary Figures

A.1. hiPSC-CM 2D monolayer quality

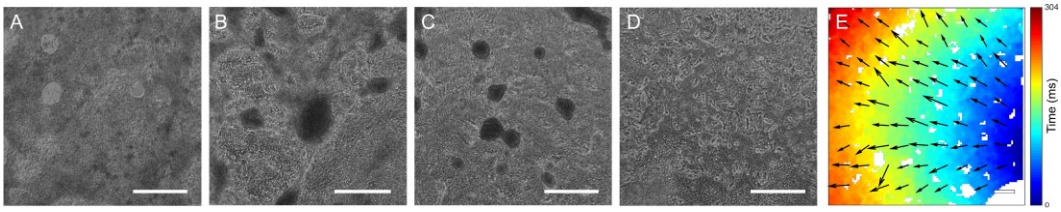

hiPSC-CM 2D monolayer quality by spontaneous beating phenotype and optical electrical mapping. A-D : Optical microscopy of 2D CM monolayer as a connected beating sheet (A), with connected beating areas (B), isolated beating areas (C) and that are not beating (D). Scale bar: 500 µm. E: Isochronal activation map of hiPSC-CM 2D monolayer by optical mapping using a voltage sensitive dye. Scale bar: 1 mm.

A.2. Cardiosphere optimization studies

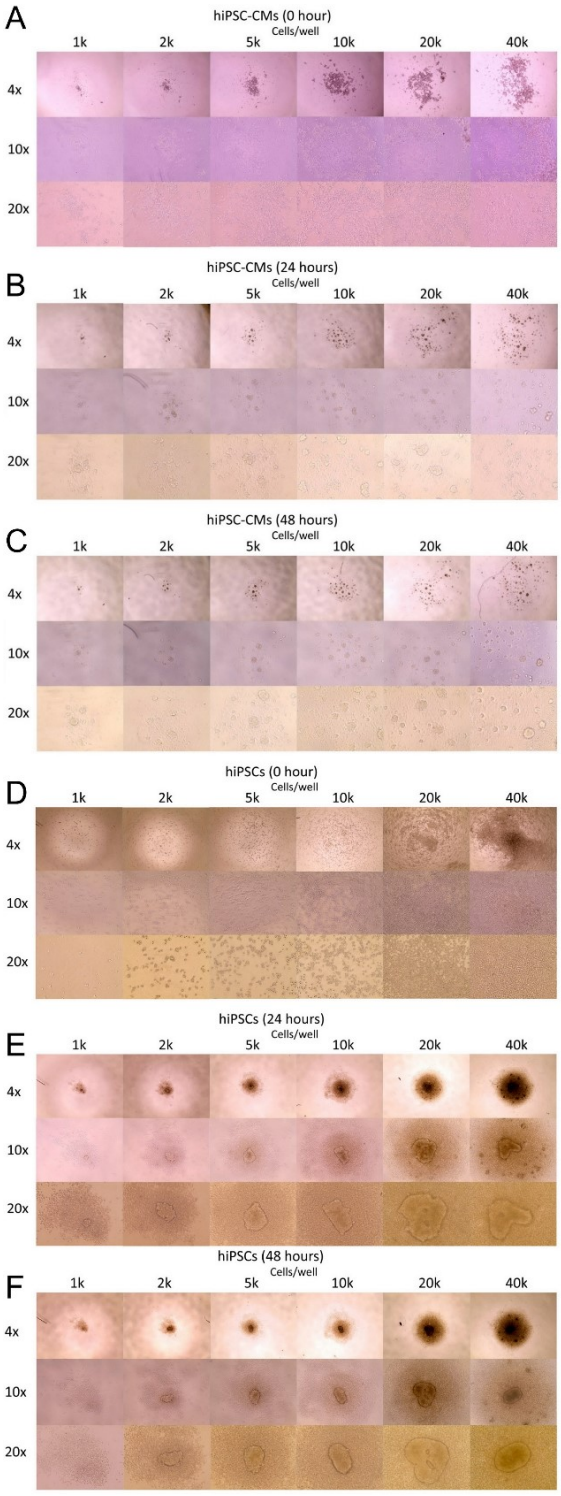

A-C: IPSCs (100%) do not form spheroids after 24 hours (B) and 48 hours (C) in ultra-low attachment 96-well plates (Top row: 4x magnification, Middle row: 10x magnification Bottom row: 20x magnification). Instead a soft gel-like cell aggregate, that is easily disrupted, forms within 24 hours. D-F: hiPSC-CMs (100%) do not form spheroids after 24 hours (B) and 48 hours (C) in ultra-low attachment 96-well plates (Top row: 4x magnification, Middle row: 10x magnification Bottom row: 20x magnification). Instead, multiple small scattered spheroids form within 24 hours, which persists at 48 hours.

A.3. Additional images of 3D bioprinted cardiac patches

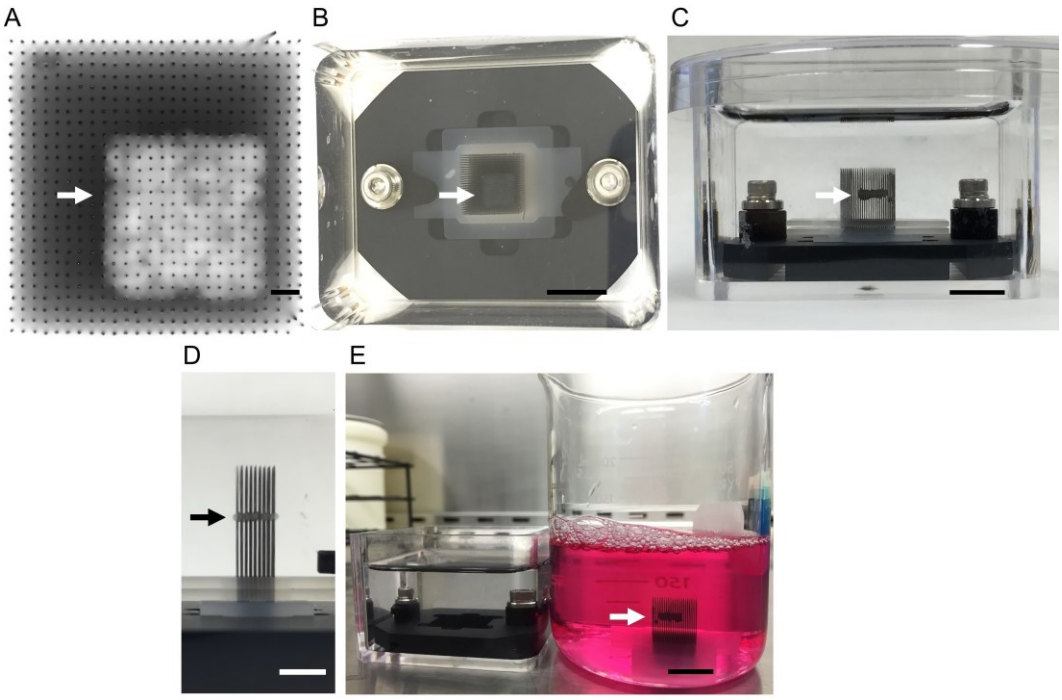

A: Top view of a 3D bioprinted cardiac patch (white arrow) on a 26 x 26 needle array. Scale bar: 1 mm. B: Top view of a 3D bioprinted cardiac patch (white arrow) on a 26 x 26 needle array. Scale bar: 10 mm. C: Side view of a 3D bioprinted cardiac patch (white arrow) on a 26 x 26 needle array. Scale bar: 10 mm. D: Side view of a 3D bioprinted cardiac patch (black arrow) on a 9 x 9 needle array. Scale bar: 4 mm. E: Side view of a 3D bioprinted cardiac patch (white arrow) on a 26 x 26 needle array after being transferred into a beaker with cell culture media. Scale bar: 10 mm.

A.4. Cardiosphere cell viability

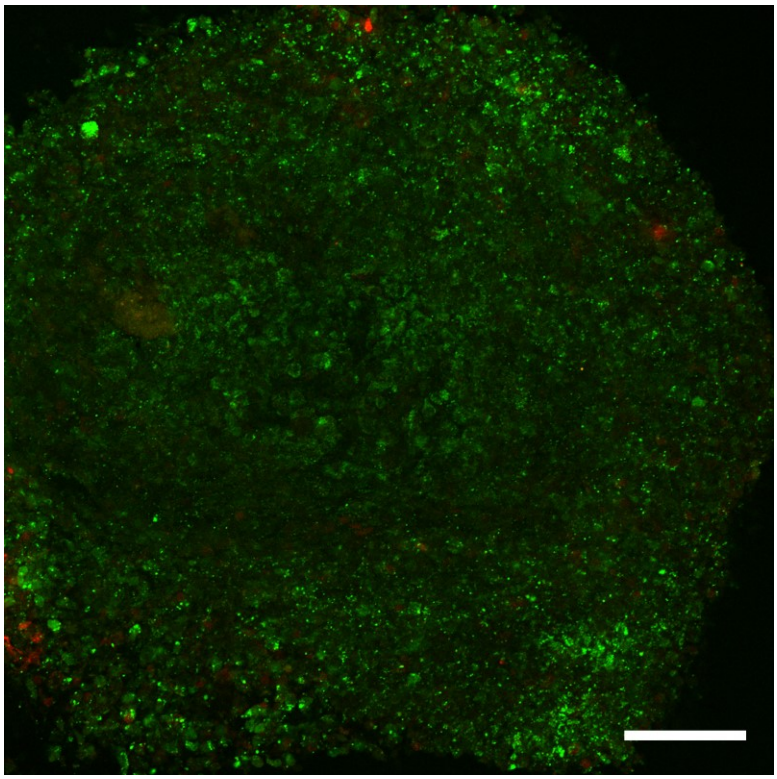

Cell viability assessment by confocal imaging of the mid-section of a cardiosphere stained with cytotoxicity kit (live cells green, dead cells red). Scale bar: 100 μm

Note: The cell viability of the cardiospheres (33,000 cells per cardiosphere, CM:FB:EC ratio 70:15:15) assessed by 3D cell viability ATP assay was 93.3%. The standard curve was generated by using cell mixtures consisting of 104, 105, 106 cells (CM:FB:EC 70:15:15).

A.5. Cell distribution in 3D bioprinted cardiac tissue

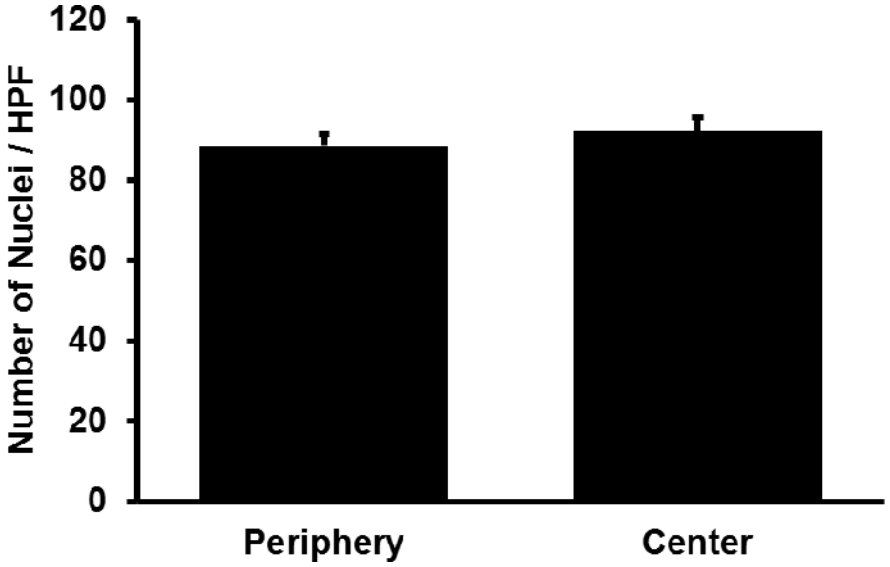

Number of nuclei per HPF (40x) of 3D bioprinted cardiac patch in the periphery: 88.5 ± 3.1 nuclei/HPF (n=4) vs. center: 92.3 ± 3.5 nuclei/HPF (n=4) (Number of nuclei/HPF ± SD) ($p = 0.16$).

A.6. Electrophysiological studies of calmodulinopathic 2D monolayers

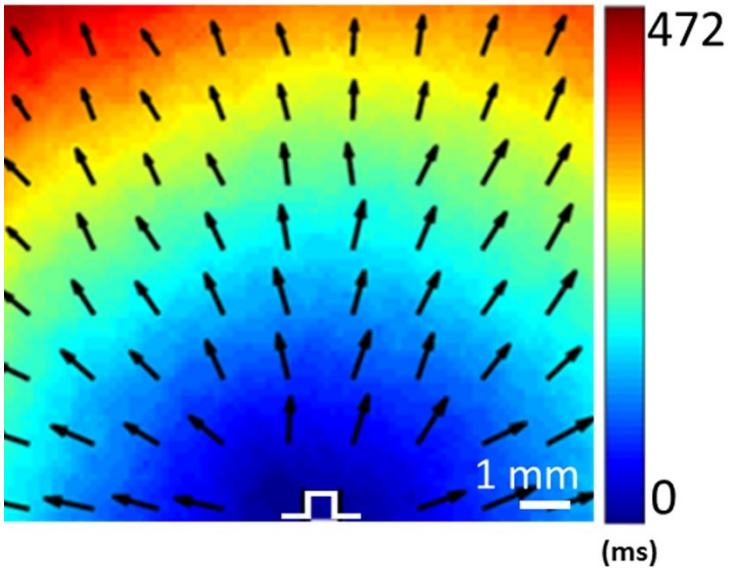

Activation map of D130G-CALM2 2D hiPSC-CM monolayer. Scale bar: 1mm.

Videos

B.1. Biomaterial-free 3D bioprinting instructional video with narration

Journal of Visualized Experiments https://www.jove.com/video/55438/creation-cardiac-tissue-exhibiting-mechanical-integration-spheroids (2)

B.2. Video microscopy of 2D CM monolayers.

A: Connected beating sheet (Grade A).

B: Connected beating areas (Grade B).

C: Isolated beating areas (Grade C).

D: Not beating (Grade D).

https://static-content.springer.com/esm/art%3A10.1038%2Fs41598-017-05018-4/MediaObjects/41598_2017_5018_MOESM3_ESM.mov (3)

B.3. Representative optical mapping video of 3D bioprinted cardiac patch (CM:FB:EC 45:40:15). Top: 3D bioprinted cardiac patch. Middle: Action potential recording at the magenta dot in the 3D bioprinted cardiac patch. Bottom: Pacing stimulus (Pacing cycle length 2000 ms). Scale bar: 500 μm. https://static-content.springer.com/esm/art%3A10.1038%2Fs41598-017-05018-4/MediaObjects/41598_2017_5018_MOESM2_ESM.mov (3)

B.4. VR (Congenital Heart Disease Case 1)

https://onlinelibrary.wiley.com/action/downloadSupplement?doi=10.1111%2Fchd.12587&file=chd12587-sup-0001-suppinfo1.mp4 (8)

B.5. VR (Congenital Heart Disease Case 2)

https://onlinelibrary.wiley.com/action/downloadSupplement?doi=10.1111%2Fchd.12587&file=chd12587-sup-0002-suppinfo2.mp4 (8)

B.6. VR (Vascular Disease): Visualization of the right carotid pseudoaneurysm using an interactive VR system (9)

B.7. VR (Fetal Therapy) (10)

References

1. Ong CS, Pitaktong I, Hibino N. Principles of spheroid preparation for creation of 3d cardiac tissue using biomaterial-free bioprinting. In: Crook J, ed. 3-d bioprinting: Principles & protocols: Springer Nature;2019.

2. Ong CS, Fukunishi T, Nashed A et al. Creation of cardiac tissue exhibiting mechanical integration of spheroids using 3d bioprinting. J Vis Exp 2017(125).

3. Ong CS, Fukunishi T, Zhang H et al. Biomaterial-free three-dimensional bioprinting of cardiac tissue using human induced pluripotent stem cell derived cardiomyocytes. Scientific Reports 2017.

4. Yeung E, Fukunishi T, Bai Y et al. 3d printed cardiac patch augments angiogenesis and reduces scar tissue formation in vivo. Southern Thoracic Surgical Association 65th Annual Meeting. Amelia Island, FL;2018.

5. Ong CS, Fukunishi T, Pitaktong I et al. Cardiac remuscularization using 3d bioprinted cardiac patches. Circulation 2017;136(Suppl 1):A15589-A15589.

6. Ong CS, Fukunishi T, Zhang H et al. Improvement of electrophysiological and morphological characteristics of 3d bioprinted human induced pluripotent stem cell-derived cardiac patches by defined factors. Congenital Heart Surgeons' Society Annual Meeting. Chicago, IL;2017.

7. Ong CS, Huang CY, Han J et al. Crispr interference to correct diseased 2d and 3d hipsc-cms with calmodulinopathies. Circulation 2018;138(Suppl 1):A11569-A11569.

8. Ong CS, Krishnan A, Huang CY et al. Role of virtual reality in congenital heart disease. Congenital heart disease 2018;13(3):357-361.

9. Ong CS, Deib G, Yesantharao P et al. Virtual reality in neurointervention. Journal of vascular and interventional neurology 2018;10(1):17-22.

10. Ong C, Faden M, Baschat AA, Garcia J, Miller JL. Oc05.03: Virtual reality projection of fetal cardiac anomalies from three-dimensional prenatal ultrasound data. Ultrasound in Obstetrics & Gynecology 2018;52(S1):10-10.

11. Limpitikul WB, Dick IE, Tester DJ et al. A precision medicine approach to the rescue of function on malignant calmodulinopathic long-qt syndrome. Circulation research 2017;120(1):39-48.

12. Laschke MW, Menger MD. Life is 3d: Boosting spheroid function for tissue engineering. Trends in Biotechnology;35(2):133-144.

13. Ong CS, Zhou X, Han J et al. In vivo therapeutic applications of cell spheroids. Biotechnology Advances 2018;36(2):494-505.

14. Ong CS, Fukunishi T, Nashed A et al. Creation of cardiac tissue exhibiting mechanical integration of spheroids using 3d bioprinting. Journal of Visualized Experiments 2017:e55438.

15. Itoh M, Nakayama K, Noguchi R et al. Scaffold-free tubular tissues created by a bio-3d printer undergo remodeling and endothelialization when implanted in rat aortae. PloS one 2015;10(9):e0136681.

16. Yurie H, Ikeguchi R, Aoyama T et al. The efficacy of a scaffold-free bio 3d conduit developed from human fibroblasts on peripheral nerve regeneration in a rat sciatic nerve model. PloS one 2017;12(2):e0171448.

17. Kizawa H, Nagao E, Shimamura M, Zhang G, Torii H. Scaffold-free 3d bio-printed human liver tissue stably maintains metabolic functions useful for drug discovery. Biochemistry and Biophysics Reports 2017;10:186-191.

18. Moldovan L, Barnard A, Gil CH et al. Ipsc-derived vascular cell spheroids as building blocks for scaffold-free biofabrication. Biotechnol J 2017.

19. Moldovan NI, Hibino N, Nakayama K. Principles of the kenzan method for robotic cell spheroid-based three-dimensional bioprinting. Tissue engineering Part B, Reviews 2017;23(3):237-244.

20. Heidenreich PA, Albert NM, Allen LA et al. Forecasting the impact of heart failure in the united states: A policy statement from the american heart association. Circulation Heart failure 2013;6(3):606-619.

21. Udelson JE, Stevenson LW. The future of heart failure diagnosis, therapy, and management. Circulation 2016;133(25):2671-2686.

22. Oh H, Ito H, Sano S. Challenges to success in heart failure: Cardiac cell therapies in patients with heart diseases. Journal of cardiology 2016;68(5):361-367.

23. Sanganalmath SK, Bolli R. Cell therapy for heart failure: A comprehensive overview of experimental and clinical studies, current challenges, and future directions. Circulation research 2013;113(6):810-834.

24. Michler RE. Stem cell therapy for heart failure. Cardiology in review 2014;22(3):105-116.

25. Huang P, Tian X, Li Q, Yang Y. New strategies for improving stem cell therapy in ischemic heart disease. Heart failure reviews 2016;21(6):737-752.

26. Patel AN, Mittal S, Turan G et al. Revive trial: Retrograde delivery of autologous bone marrow in patients with heart failure. Stem cells translational medicine 2015;4(9):1021-1027.

27. Martino H, Brofman P, Greco O et al. Multicentre, randomized, double-blind trial of intracoronary autologous mononuclear bone marrow cell injection in non-ischaemic dilated cardiomyopathy (the dilated cardiomyopathy arm of the miheart study). European heart journal 2015;36(42):2898-2904.

28. Guijarro D, Lebrin M, Lairez O et al. Intramyocardial transplantation of mesenchymal stromal cells for chronic myocardial ischemia and impaired left ventricular function: Results of the mesami 1 pilot trial. International journal of cardiology 2016;209:258-265.

29. Wang F, Guan J. Cellular cardiomyoplasty and cardiac tissue engineering for myocardial therapy. Advanced drug delivery reviews 2010;62(7-8):784-797.

30. Murphy SV, Atala A. 3d bioprinting of tissues and organs. Nature biotechnology 2014;32(8):773-785.

31. Smith AS, Macadangdang J, Leung W, Laflamme MA, Kim DH. Human ipsc-derived cardiomyocytes and tissue engineering strategies for disease modeling and drug screening. Biotechnology advances 2017;35(1):77-94.

32. Bobak M, Guanglei X, Simon D, James KM. Current progress in 3d printing for cardiovascular tissue engineering. Biomedical Materials 2015;10(3):034002.

33. Yeong WY, Sudarmadji N, Yu HY et al. Porous polycaprolactone scaffold for cardiac tissue engineering fabricated by selective laser sintering. Acta Biomater 2010;6(6):2028-2034.

34. Gaetani R, Doevendans PA, Metz CH et al. Cardiac tissue engineering using tissue printing technology and human cardiac progenitor cells. Biomaterials 2012;33(6):1782-1790.

35. Gao L, Kupfer M, Jung J et al. Myocardial tissue engineering with cells derived from human induced-pluripotent stem cells and a native-like, high-resolution, 3-dimensionally printed scaffold. Circulation research 2017.

36. Pati F, Jang J, Ha DH et al. Printing three-dimensional tissue analogues with decellularized extracellular matrix bioink. Nature communications 2014;5:3935.

37. Norotte C, Marga FS, Niklason LE, Forgacs G. Scaffold-free vascular tissue engineering using bioprinting. Biomaterials 2009;30(30):5910-5917.

38. Lian X, Hsiao C, Wilson G et al. Robust cardiomyocyte differentiation from human pluripotent stem cells via temporal modulation of canonical wnt signaling. Proceedings of the National Academy of Sciences 2012;109(27):E1848–E1857.

39. Little MA, Jones NS. Sparse bayesian step-filtering for high-throughput analysis of molecular machine dynamics. Quantitative Biology 2010.

40. Chartrand R. Numerical differentiation of noisy, nonsmooth data. ISRN Applied Mathematics 2011;2011:11.

41. Uosaki H, Fukushima H, Takeuchi A et al. Efficient and scalable purification of cardiomyocytes from human embryonic and induced pluripotent stem cells by vcam1 surface expression. PLoS ONE 2011;6(8):e23657.

42. Noguchi R, Nakayama K, Itoh M et al. Development of a three-dimensional pre-vascularized scaffold-free contractile cardiac patch for treating heart disease. The Journal of heart and lung transplantation : the official publication of the International Society for Heart Transplantation 2016;35(1):137-145.

43. Zhu R, Blazeski A, Poon E, Costa KD, Tung L, Boheler KR. Physical developmental cues for the maturation of human pluripotent stem cell-derived cardiomyocytes. Stem cell research & therapy 2014;5(5):117.

44. Zhu R, Millrod MA, Zambidis ET, Tung L. Variability of action potentials within and among cardiac cell clusters derived from human embryonic stem cells. Scientific reports 2016;6:18544.

45. Matsuura K, Utoh R, Nagase K, Okano T. Cell sheet approach for tissue engineering and regenerative medicine. Journal of controlled release : official journal of the Controlled Release Society 2014;190:228-239.

46. Masumoto H, Sakata R. Cardiovascular surgery for realization of regenerative medicine. General thoracic and cardiovascular surgery 2012;60(11):744-755.

47. Masuda S, Shimizu T. Three-dimensional cardiac tissue fabrication based on cell sheet technology. Advanced drug delivery reviews 2016;96:103-109.

48. Sakaguchi K, Shimizu T, Okano T. Construction of three-dimensional vascularized cardiac tissue with cell sheet engineering. Journal of controlled release : official journal of the Controlled Release Society 2015;205:83-88.

49. Martin I, Wendt D, Heberer M. The role of bioreactors in tissue engineering. Trends in biotechnology 2004;22(2):80-86.

50. Chiu LL, Iyer RK, Reis LA, Nunes SS, Radisic M. Cardiac tissue engineering: Current state and perspectives. Frontiers in bioscience (Landmark edition) 2012;17:1533-1550.

51. Stevens KR, Pabon L, Muskheli V, Murry CE. Scaffold-free human cardiac tissue patch created from embryonic stem cells. Tissue engineering Part A 2009;15(6):1211-1222.

52. Stevens KR, Kreutziger KL, Dupras SK et al. Physiological function and transplantation of scaffold-free and vascularized human cardiac muscle tissue. Proceedings of the National Academy of Sciences 2009;106(39):16568-16573.

53. Rogozhnikov D, O'Brien PJ, Elahipanah S, Yousaf MN. Scaffold free bio-orthogonal assembly of 3-dimensional cardiac tissue via cell surface engineering. Scientific reports 2016;6:39806.

54. Hirt MN, Hansen A, Eschenhagen T. Cardiac tissue engineering: State of the art. Circulation research 2014;114(2):354-367.

55. Borovjagin AV, Ogle BM, Berry JL, Zhang J. From microscale devices to 3d printing: Advances in fabrication of 3d cardiovascular tissues. Circulation research 2017;120(1):150-165.

56. Lee JH, Han YS, Lee SH. Long-duration three-dimensional spheroid culture promotes angiogenic activities of adipose-derived mesenchymal stem cells. Biomolecules & therapeutics 2016;24(3):260-267.

57. Kelm JM, Ehler E, Nielsen LK, Schlatter S, Perriard JC, Fussenegger M. Design of artificial myocardial microtissues. Tissue Eng 2004;10(1-2):201-214.

58. Trieschmann J, Bettin D, Haustein M et al. The interaction between adult cardiac fibroblasts and embryonic stem cell-derived cardiomyocytes leads to proarrhythmic changes in in vitro cocultures. Stem cells international 2016;2016:2936126.

59. Zhou P, Pu WT. Recounting cardiac cellular composition. Circulation Research 2016;118(3):368-370.

60. Pinto AR, Ilinykh A, Ivey MJ et al. Revisiting cardiac cellular composition. Circulation Research 2016;118(3):400-409.

61. Morrissette-McAlmon J, Blazeski A, Somers S, Kostecki G, Tung L, Grayson WL. Adipose-derived perivascular mesenchymal stromal/stem cells promote functional vascular tissue engineering for cardiac regenerative purposes. Journal of tissue engineering and regenerative medicine 2017:n/a-n/a.

62. Carvalho E, Verma P, Hourigan K, Banerjee R. Myocardial infarction: Stem cell transplantation for cardiac regeneration. Regenerative medicine 2015;10(8):1025-1043.

63. Cambria E, Pasqualini FS, Wolint P et al. Translational cardiac stem cell therapy: Advancing from first-generation to next-generation cell types. npj Regenerative Medicine 2017;2(1):17.

64. Ye L, Zimmermann WH, Garry DJ, Zhang J. Patching the heart: Cardiac repair from within and outside. Circulation research 2013;113(7):922-932.

65. Ong CS, Zhou X, Huang CY, Fukunishi T, Zhang H, Hibino N. Tissue engineered vascular grafts: Current state of the field. Expert review of medical devices 2017;14(5):383-392.

66. Ong CS, Yesantharao P, Huang CY et al. 3d bioprinting using stem cells. Pediatric research 2018;83(1-2):223-231.

67. Dor V, Di Donato M, Sabatier M, Montiglio F, Civaia F. Left ventricular reconstruction by endoventricular circular patch plasty repair: A 17-year experience. Seminars in thoracic and cardiovascular surgery 2001;13(4):435-447.

68. Pok S, Stupin IV, Tsao C et al. Full-thickness heart repair with an engineered multilayered myocardial patch in rat model. Advanced healthcare materials 2017;6(5).

69. Duran AG, Reidell O, Stachelscheid H et al. Regenerative medicine/cardiac cell therapy: Pluripotent stem cells. The Thoracic and cardiovascular surgeon 2018;66(1):53-62.

70. Kannan S, Kwon C. Regulation of cardiomyocyte maturation during critical perinatal window. The Journal of physiology 2018.

71. Mummery CL. Perspectives on the use of human induced pluripotent stem cell-derived cardiomyocytes in biomedical research. Stem cell reports 2018;11(6):1306-1311.

72. Birket MJ, Ribeiro MC, Kosmidis G et al. Contractile defect caused by mutation in mybpc3 revealed under conditions optimized for human psc-cardiomyocyte function. Cell reports 2015;13(4):733-745.

73. Makita N, Yagihara N, Crotti L et al. Novel calmodulin mutations associated with congenital arrhythmia susceptibility. Circulation Cardiovascular genetics 2014;7(4):466-474.

74. Crotti L, Johnson CN, Graf E et al. Calmodulin mutations associated with recurrent cardiac arrest in infants. Circulation 2013;127(9):1009-1017.

75. Qi LS, Larson MH, Gilbert LA et al. Repurposing crispr as an rna-guided platform for sequence-specific control of gene expression. Cell 2013;152(5):1173-1183.

76. Gilbert LA, Larson MH, Morsut L et al. Crispr-mediated modular rna-guided regulation of transcription in eukaryotes. Cell 2013;154(2):442-451.

77. Yanamandala M, Zhu W, Garry DJ et al. Overcoming the roadblocks to cardiac cell therapy using tissue engineering. Journal of the American College of Cardiology 2017;70(6):766.

78. Benam KH, Dauth S, Hassell B et al. Engineered in vitro disease models. Annual Review of Pathology: Mechanisms of Disease 2015;10(1):195-262.

79. Strauss DG, Blinova K. Clinical trials in a dish. Trends in Pharmacological Sciences 2017;38(1):4-7.

80. Nie J, Hashino E. Organoid technologies meet genome engineering. EMBO reports 2017;18(3):367-376.

81. Driehuis E, Clevers H. Crispr/cas 9 genome editing and its applications in organoids. American Journal of Physiology-Gastrointestinal and Liver Physiology 2017;312(3):G257-G265.

82. Ong CS, Fukunishi T, Zhang H et al. Biomaterial-free three-dimensional bioprinting of cardiac tissue using human induced pluripotent stem cell derived cardiomyocytes. Sci Rep 2017;7(1):4566.

83. Schwank G, Koo BK, Sasselli V et al. Functional repair of cftr by crispr/cas9 in intestinal stem cell organoids of cystic fibrosis patients. Cell stem cell 2013;13(6):653-658.

84. Pulgarin DAV, Nyberg WA, Bowlin GL, Espinosa A. Crispr/cas systems in tissue engineering: A succinct overview of current use and future opportunities. Curr Trends Biomedical Eng & Biosci 2017;5(4):555670.

85. Park S, Lui C, Jung W-H et al. Mechanical characterization of hipsc-derived cardiac tissues for quality control. Advanced Biosystems 2018;2(12):1800251.

86. Zimmerman TG, Lanier J, Blanchard C, Bryson S, Harvill Y. A hand gesture interface device. SIGCHI Bull 1986;18(4):189-192.

87. Pensieri C, Pennacchini M. Overview: Virtual reality in medicine. 2014 2014;7(1).

88. Chinnock C. Virtual reality in surgery and medicine. Hospital technology series 1994;13(18):1-48.

89. Bao X, Mao Y, Lin Q et al. Mechanism of kinect-based virtual reality training for motor functional recovery of upper limbs after subacute stroke. Neural Regeneration Research 2013;8(31):2904-2913.

90. Yiannakopoulou E, Nikiteas N, Perrea D, Tsigris C. Virtual reality simulators and training in laparoscopic surgery. International journal of surgery (London, England) 2015;13:60-64.

91. Yoo S-J. 3d printing in medicine of congenital heart diseases. 3D Print Med 2015;2.

92. Hibino N. Three dimensional printing: Applications in surgery for congenital heart disease. World journal for pediatric & congenital heart surgery 2016;7(3):351-352.

93. Vukicevic M, Mosadegh B, Min JK, Little SH. Cardiac 3d printing and its future directions. JACC Cardiovascular imaging 2017;10(2):171-184.

94. Wierzbicki M, Drangova M, Guiraudon G, Peters T. Validation of dynamic heart models obtained using non-linear registration for virtual reality training, planning, and guidance of minimally invasive cardiac surgeries. Medical image analysis 2004;8(3):387-401.

95. Kim Y, Kim H, Kim YO. Virtual reality and augmented reality in plastic surgery: A review. Archives of plastic surgery 2017;44(3):179-187.

96. Ripley B, Kelil T, Cheezum MK et al. 3d printing based on cardiac ct assists anatomic visualization prior to transcatheter aortic valve replacement. Journal of cardiovascular computed tomography 2016;10(1):28-36.

97. Ong CS, Loke YH, Opfermann J et al. Virtual surgery for conduit reconstruction of the right ventricular outflow tract. World journal for pediatric & congenital heart surgery 2017;8(3):391-393.

98. Linte CA, Moore J, Wedlake C et al. Inside the beating heart: An in vivo feasibility study on fusing pre- and intra-operative imaging for minimally invasive therapy. International journal of computer assisted radiology and surgery 2009;4(2):113-123.

99. Mitsouras D. Medical 3d printing for the radiologist. RadioGraphics 2015;35.

100. Olivieri LJ, Krieger A, Loke YH, Nath DS, Kim PC, Sable CA. Three-dimensional printing of intracardiac defects from three-dimensional echocardiographic images: Feasibility and relative accuracy. J Am Soc Echocardiogr 2015;28(4):392-397.

101. Farooqi KM, Sengupta PP. Echocardiography and three-dimensional printing: Sound ideas to touch a heart. J Am Soc Echocardiogra 2015;28.

102. Mahmood F, Owais K, Taylor C et al. Three-dimensional printing of mitral valve using echocardiographic data. JACC Cardiovascular imaging 2015;8(2):227-229.

103. Stepan K, Zeiger J, Hanchuk S et al. Immersive virtual reality as a teaching tool for neuroanatomy. International forum of allergy & rhinology 2017;7(10):1006-1013.

104. Marks SC. Recovering the significance of 3-dimensional data in medical education and clinical practice. Clin Anat 2001;14(1):90-91.

105. Beck J, Rohde S, el Beltagy M et al. Difference in configuration of ruptured and unruptured intracranial aneurysms determined by biplanar digital subtraction angiography. Acta Neurochir 2003;145(10):861-865.

106. Hademenos GJ, Massoud TF, Turjman F, Sayre JW. Anatomical and morphological factors correlating with rupture of intracranial aneurysms in patients referred for endovascular treatment. Neuroradiology 1998;40(11):755-760.

107. Lall RR, Eddleman CS, Bendok BR, Batjer HH. Unruptured intracranial aneurysms and the assessment of rupture risk based on anatomical and morphological factors: Sifting through the sands of data. Neurosurg Focus 2009;26(5).

108. Ma BS, Harbaugh RE, Raghavan ML. Three-dimensional geometrical characterization of cerebral aneurysms. Ann Biomed Eng 2004;32(2):264-273.

109. Sadatomo T, Yuki K, Migita K, Taniguchi E, Kodama Y, Kurisu K. Morphological differences between ruptured and unruptured cases in middle cerebral artery aneurysms. Neurosurgery 2008;62(3):602-608.

110. Sportillo D, Paljic A, Boukhris M, Fuchs P, Ojeda L, Roussarie V. An immersive virtual reality system for semi-autonomous driving simulation: A comparison between realistic and 6-dof controller-based interaction. Proceedings

of the 9th International Conference on Computer and Automation Engineering: ACM;2017. p. 6-10.

111. Slater M. Place illusion and plausibility can lead to realistic behaviour in immersive virtual environments. Philosophical transactions of the Royal Society of London Series B, Biological sciences 2009;364(1535):3549-3557.

112. Slater M. Enhancing our lives with immersive virtual reality. Frontiers in Robotics and AI 3 2016;74.

113. Sutherland IE. A head-mounted three dimensional display. Proceedings of the December 9-11, 1968, Fall Joint Computer Conference, Part 1 (New York, NY:ACM), 757-764 1968.

114. Castelvecchi D. Warped worlds in virtual reality. Nature 2017;543(7646):473-473.

115. Sousa M MD, Paulo S, Matela N, JOrge J, Lopes DS. Vrrrroom: Virtual reality for radiologists in the reading room. In Proceedings of the 2017 CHI Conference on Human Factors in Computing Systems 2017:4057-4062.

116. 2018 Fetal cardiac abnormalities: Screening, evaluation, and pregnancy management - uptodate. Available at https://www.uptodate.com/contents/fetal-cardiac-abnormalities-screening-evaluation-and-pregnancy-management.

117. 2014 Deaths: Leading causes for 2014. Available at https://www.uptodate.com/contents/fetal-cardiac-abnormalities-screening-evaluation-and-pregnancy-management/abstract/1.

118. Carvalho JS, Ho SY, Shinebourne EA. Sequential segmental analysis in complex fetal cardiac abnormalities: A logical approach to diagnosis - carvalho - 2005 - ultrasound in obstetrics & gynecology - wiley online library. 26 2005(105-111).

119. Rajiah P, Mak C, Dubinksy TJ, Dighe M. Ultrasound of fetal cardiac anomalies. American Journal of Roentgenology 2011;197(4).

120. Kleinman CS, Donnerstein RL, DeVore GR et al. Fetal echocardiography for evaluation of in utero congestive heart failure. The New England Journal of Medicine 2010;306:568-575.

121. Small M, Copel JA. Indications for fetal echocardiography | springerlink. Pediatric Cardiology 2004;25(3):210-222.

122. 2018 Detection of a heart defect in the fetus. Available at http://www.heart.org/HEARTORG/Conditions/CongenitalHeartDefects/SymptomsDiagnosisofCongenitalHeartDefects/Detection-of-a-Heart-Defect-in-the-Fetus_UCM_315673_Article.jsp#.Wv-kJlMvxE4.

123. Yuan SM. Fetal cardiac interventions: An update of therapeutic options. Rev Bras Cir Cardiovasc 2014;29(3):388-395.

124. Tworetzky W, McElhinney DB, Reddy VM, Brook MM, Hanley FL, Silverman NH. Improved surgical outcome after fetal diagnosis of hypoplastic left heart syndrome. Circulation 2001;103:1269-1273.

125. Lee W, Comstock CH. Prenatal diagnosis of congenital heart disease: Where are we now? Ultrasound Clinics 2006;1(2):273-291.

126. Schultheis MT, Rizzo AA. The application of virtual reality technology in rehabilitation. Rehabilitation Psychology 2001;46(3):296-311.

127. Wiederhold BK, Wiederhold MD. Virtual reality therapy for anxiety disorders: Advances in evaluation and treatment.; 2005.

128. Laver K, George S, Thomas S, Deutsch JE, Crotty M. Virtual reality for stroke rehabilitation. Stroke 2012.

129. Reddy UM, Filly RA, Copel JA. Prenatal imaging: Ultrasonography and magnetic resonance imaging. Obstet Gynecol 2008;112(1):145-157.

130. Gallagher AG, Cates CU. Virtual reality training for the operating room and cardiac catheterisation laboratory. The Lancet 2004;364(9444):1538-1540.

131. Vining DJ, From the Department of Radiology B-GSoM, Winston-Salem, NC, Liu K et al. Virtual bronchoscopy: Relationships of virtual reality endobronchial simulations to actual bronchoscopic findings. CHEST 1996;109(2):549-553.

132. Qui T-m, Zhang Y, Wu J-S et al. Virtual reality presurgical planning for cerebral gliomas adjacent to motor pathways in an integrated 3-d stereoscopic visualization of structural mri and dti tractography | springerlink. Acta Neurochirurgica 2010.

133. Marescaux J, Clément JM, Tassetti V et al. Virtual reality applied to hepatic surgery simulation: The next revolution. Ann Surg 1998;228(5):627-634.

134. J X, N S, RW Y et al. Three-dimensional virtual reality surgical planning and simulation workbench for orthognathic... - abstract - europe pmc. Europe PMC 2000;15(4):265-282.

135. Stadie A, Kockro R, Reisch R. Virtual reality system for planning minimally invasive neurosurgery. Journal of Neurosurgery 2008;108(2):382-394.

Biography

Dr. Chin Siang Ong was born in Singapore. He obtained his medical degree (MBBS) from the Yong Loo Lin School of Medicine, National University of Singapore in 2010. He subsequently joined the National University Health System (NUHS) (Singapore) General Surgery Residency Program, before joining the NUHS Cardiothoracic Surgery Residency Program. During this time, he also served as a Medical Officer in the Singapore Civil Defence Force (Rank: Captain (Dr)), as well as a volunteer doctor in humanitarian relief missions to the Philippines with the International Committee of the Red Cross and the Singapore Red Cross.

In August 2015, Chin Siang began his PhD in Cellular and Molecular Medicine at the Johns Hopkins School of Medicine in Baltimore, Maryland, USA. During his PhD, he was awarded the John A. Hawkins Top Scoring Abstract Award at the Congenital Heart Surgeons' Society Annual Meeting (2016), the American Heart Association (AHA) Council on Cardiovascular Surgery and Anesthesia Top Ten Abstract Travel Grant Award (2016), the 23rd Annual Talalay-Gott Cardiac Research Prize (2017) ("Awarded annually to a cardiac surgical research resident at Johns Hopkins Medical Institutions for the most outstanding research by a resident during that particular year"), the Johns Hopkins Graduate Student

Association (GSA) Memorial Cash Prize and the Johns Hopkins GSA Student Travel Award (2017). He was also awarded the Tan Kah Kee Postgraduate Scholarship and the AHA Predoctoral Fellowship (Priority Score: 1.39. Percentile Rank: 0.25%. Cut-off: 19.90%) in 2017.

After completing his PhD, Chin Siang will be starting a research fellowship in the Division of Cardiac Surgery at the Massachusetts General Hospital, Harvard Medical School in Boston, Massachusetts, USA, from April 2019.